
DRAFT

CMS Paper

The content of this note is intended for CMS internal use and distribution only

2016/08/01

Head Id:

Archive Id: 362028P

Archive Date: 2016/08/01

Archive Tag: trunk

A search for new phenomena at 13 TeV in final states with one or more jets and missing transverse momentum with the α_T variable

The CMS Collaboration

Abstract

A search for new-physics phenomena is performed in final states containing one or more jets and an imbalance in transverse momentum in pp collisions at a centre-of-mass energy of 13 TeV. The analysed data sample, recorded with the CMS detector at the CERN Large Hadron Collider, corresponds to an integrated luminosity of 2.3 fb^{-1} . Several kinematic variables are employed to suppress the dominant background, multijet production from quantum chromodynamics, as well as discriminate effectively between other standard model and new-physics processes. The search provides sensitivity to a broad range of the new-physics models that yield a stable weakly interacting massive particle. The observed candidate events are found to agree with the expected contributions from standard model processes, and the result is interpreted in the mass parameter space of fourteen simplified supersymmetric models that assume the pair production of gluinos or squarks, and a range of decay modes. For models that assume the pair production of gluinos, masses up to 1575 GeV and 975 GeV are excluded for gluinos and neutralinos, respectively. For models involving the pair production of top squarks and compressed mass spectra, top squark masses up to 400 GeV are excluded.

This box is only visible in draft mode. Please make sure the values below make sense.

PDFAuthor: Mark Baber, Robert Bainbridge, Freya Blekman, Oliver Buchmueller, Stefano Casasso, Matthew Citron, Adam Elwood, Henning Flaecher, Aran Garcia-Bellido, Christian Laner, Kin Ho Lo, Sarah Alam Malik, Bjoern Penning, Tai Sakuma, Dominic Smith, Alex Tapper

PDFTitle: An inclusive search for new phenomena at 13 TeV in final states with one or more jets and missing transverse momentum with the AlphaT variable

PDFSubject: CMS

PDFKeywords: CMS, jets, missing transverse momentum, supersymmetry, dark matter, AlphaT

Please also verify that the abstract does not use any user defined symbols

DRAFT

1 Introduction

The standard model (SM) of particle physics is successful in describing a wide range of phenomena and the model is currently being extensively tested at high energies with collider-based experiments. To date, no contrary evidence has yet been attained. Nevertheless, the SM is widely believed to be only an effective approximation of a more complete theory that supersedes it at a higher energy scale. Supersymmetry (SUSY) [1–4] is a complete, renormalisable extension to the Standard Model (SM) that extends the space-time symmetry group underpinning the SM. For each boson (fermion) in the SM, a fermionic (bosonic) superpartner, which differs in spin by one-half unit, is introduced.

The proposed supersymmetric extension to the SM is compelling from theoretical, phenomenological, and experimental considerations. From a theory perspective, the addition of superpartners to SM particles can modify the running of the gauge coupling constants such that their unification can be achieved at a high scale [5–7]. Experimentally, SUSY is testable through the prediction of an extensive array of new observable states (of unknown masses) [8, 9]. The gluinos \tilde{g} , light- and heavy-flavour squarks $\tilde{q}, \tilde{b}, \tilde{t}$, and sleptons $\tilde{\ell}$ are, respectively, the superpartners to gluons, quarks, and leptons. An extended Higgs sector is also predicted, as well as four neutralino $\tilde{\chi}_{1,2,3,4}^0$ and two chargino $\tilde{\chi}_{1,2}^\pm$ states that arise from the mixing between the superpartner states to neutral and charged Higgs bosons and the electroweak gauge bosons.

A more topical perspective, given the recently discovered Higgs boson [10, 11], is the conjecture that the superpartners (“sparticles”) can alleviate the gauge hierarchy problem of the SM, by compensating for radiative corrections to the Higgs mass from loop processes involving SM particles [12, 13]. These corrections diverge according to a power-law dependence on scale, which can only be accommodated in the SM through an extreme level of fine tuning of the bare Higgs mass parameter. A “natural” solution, with minimal fine-tuning, requires the $\tilde{t}_L, \tilde{t}_R, \tilde{b}_L$, and \tilde{g} to be realised at or near the electroweak scale [14]. These “natural” constraints, which can be relaxed at the expense of some level of fine tuning, imply the presence of states accessible by the CERN Large Hadron Collider (LHC).

Finally, the assumption of R-parity conservation [15] has important consequences for cosmology and collider phenomenology. SUSY particles are expected to be produced in pairs at the LHC, with heavy states decaying to the lightest stable supersymmetric particle (LSP). The LSP is generally assumed to be the $\tilde{\chi}_1^0$, which is weakly interacting and massive. This sparticle is considered to be a Dark Matter (DM) candidate [16], the existence of which is supported by astrophysical data [17]. Hence, the characteristic signature of “natural” SUSY production at the LHC is a final state containing an abundance of jets, possibly originating from top or bottom quarks, accompanied by a significant transverse momentum imbalance, \vec{p}_T^{miss} .

The lack of evidence to date for SUSY has also focused the attention on regions of the parameter space with weak coverage, which includes “natural” models [18–22]. For example, models in which both the \tilde{t} and the $\tilde{\chi}_1^0$ are light and nearly degenerate in mass are phenomenologically well motivated [23–26]. This class of models, with “compressed” mass spectra, typically yield SM particles with very low momenta from the decays of sparticles. Hence, searches rely on the associated production of jets, often resulting from initial-state radiation (ISR), to achieve nonnegligible experimental acceptance.

This article presents an inclusive search for new-physics phenomena in hadronic final states with one or more energetic jets and an imbalance in transverse momentum, performed in pp collisions at a centre-of-mass energy $\sqrt{s} = 13 \text{ TeV}$. The analysed data sample corresponds to an integrated luminosity of $2.3 \pm 0.1 \text{ fb}^{-1}$ collected by the Compact Muon Solenoid (CMS)

experiment. Previous iterations of this search have been performed in pp collisions at both $\sqrt{s} = 7$ [27–29] and 8 TeV [30, 31].

The increase in the centre-of-mass energy of the LHC, from $\sqrt{s} = 8$ to 13 TeV, provides a unique opportunity to search for the characteristic signatures of new physics at the TeV scale. For example, the increase in \sqrt{s} leads to a factor $\gtrsim 35$ increase in the parton luminosity [32] for the pair production of coloured supersymmetric particles, each of mass 1.5 TeV, which were beyond the reach of searches performed at $\sqrt{s} = 8$ TeV [33–35]. Several searches have already provided results with the first data, interpreted within the context of SUSY, at this new energy frontier [36–39].

To ensure sensitivity to the broadest possible region of the supersymmetric parameter space, an inclusive strategy is adopted, which focuses on maintaining high acceptance, through the application of selection criteria with the lowest possible thresholds, and the categorisation of candidate signal events according to multiple discriminating variables. The search is sufficiently generic and inclusive to provide sensitivity to a wide range of nonsupersymmetric models that postulate the existence of a stable, weakly interacting, massive particle, assumed to be consistent with the nature of DM. In addition to the jets + \vec{p}_T^{miss} topology, the search considers final states containing a “monojet” + \vec{p}_T^{miss} topology, which is expected to improve the sensitivity to DM particle production in pp collisions [40, 41].

This search is based on an examination of the number of reconstructed jets per event, the number of these jets identified as originating from bottom quarks, and the scalar and vector sums of transverse momenta of these jets. These variables provide sensitivity to the different production mechanisms of massive coloured sparticles at hadron colliders (i.e. squark-squark, squark-gluino, and gluino-gluino), “natural” third-generation squark signatures, and both large and small mass splittings between the parent sparticle and the LSP.

The dominant background process for a search in all-jet final states is multijet production, a manifestation of quantum chromodynamics (QCD). An accurate estimate of this background is difficult to achieve, given the lack of precise theoretical predictions for the multijet production cross section and kinematic properties. Further, the discovery potential of a search in the all-jets channel can be particularly sensitive to the uncertainties in the estimation of a nonnegligible multijet background. Hence, this search adopts a strategy that employs several variables in an attempt to reduce the multijet contribution to a low (percent) level with respect to other SM backgrounds, rather than estimate with high precision a nonnegligible contribution.

The search is built around the dimensionless kinematic variable α_T [27, 42], which provides powerful discrimination against multijet production. The α_T variable is constructed from jet-based quantities and provides discrimination between “genuine” sources of transverse momentum imbalance, from stable, weakly interacting particles, such as neutrinos or neutralinos, that escape the detector, and “fake” sources, such as the mismeasurement of jet energies. The $\Delta\phi_{\text{min}}^*$ [27] variable exploits azimuthal angular information and also provides strong rejection power against multijet events, including rare energetic events in which neutrinos carry a significant fraction of the energy of a jet, due to semileptonic decays of heavy-flavour mesons. These two variables, defined in Section 5.3, are designed to provide robust discrimination against multijet events at the energy and luminosity frontier, and very restrictive requirements on the α_T and $\Delta\phi_{\text{min}}^*$ variables are employed in this search.

The organization of this article is as follows. Sections 2 and 3 describe, respectively, the CMS apparatus and the simulated event samples. Sections 4 and 5 describe the event reconstruction and selection criteria used to identify candidate signal events and control region samples.

Section 6 provides details on the estimation of the multijet and all other SM backgrounds. Finally, the search results and interpretations, in terms of simplified supersymmetric models, are described in Sections 7 and 8, and summarised in Section 9.

2 The CMS detector

The central feature of the CMS apparatus is a superconducting solenoid of 6 m internal diameter, providing an axial magnetic field of 3.8 T. The bore of the solenoid is instrumented with several particle detection systems. A silicon pixel and strip tracker measures charged particles within the pseudorapidity range $|\eta| < 2.5$. A lead tungstate crystal electromagnetic calorimeter (ECAL), and a brass and scintillator hadron calorimeter (HCAL), each composed of a barrel and two endcap sections, extend over a pseudorapidity range $|\eta| < 3.0$. Outside the bore of the solenoid, forward calorimeters extend the pseudorapidity coverage to $|\eta| < 5.0$, and muons are measured within $|\eta| < 2.4$ by gas-ionization detectors embedded in the steel flux-return yoke outside the solenoid. A two-tier trigger system selects pp collision events of interest. The first level (L1) of the trigger system, composed of custom hardware processors, uses information from the calorimeters and muon detectors to select the most interesting events in a fixed time interval of less than 4 μ s. The high-level trigger (HLT) processor farm further decreases the event rate from around 100 kHz to less than 1 kHz, before data storage. The CMS detector is nearly hermetic, which allows for momentum-balance measurements in the plane transverse to the beam axis. A more detailed description of the CMS detector, together with a definition of the coordinate system used and the relevant kinematic variables, can be found in Ref. [43].

3 Simulated event samples

The search relies on multiple event samples, in data or generated from Monte Carlo (MC) simulations, to estimate the contributions from SM backgrounds, as described in Section 5. The dominant SM backgrounds for the search are QCD multijet production, and the associated production of jets and top-antitop ($t\bar{t}$), single top, and vector boson ($W, Z \rightarrow \nu\bar{\nu}$). Residual contributions from other processes, such as WW, WZ, ZZ (diboson) production and the associated production of $t\bar{t}$ and a vector boson (W and Z), are also considered. Other processes, such as Drell-Yan ($q\bar{q} \rightarrow Z/\gamma^* \rightarrow \ell^+\ell^-$) and γ +jets production, are also relevant for some control regions, defined in Section 5.5.

The MADGRAPH 5 aMC@NLO 2.2.2 [44] event generator code is used at leading order (LO) accuracy to produce samples of W +jets, Z +jets, γ +jets, $t\bar{t}$, and multijet events. The same code is used at next-to-leading order (NLO) accuracy to generate samples of single top (both s- and t-channel production), $WZ, ZZ, t\bar{t}W$, and $t\bar{t}Z$ events. The NLO POWHEG v2 [45, 46] generator is used to describe WW events and the Wt -channel production of single top events. The simulated samples are normalised according to production cross sections that are calculated with NLO and next-to-NLO precision [44, 46–51]. The GEANT4 [52] package is used to simulate the detector response.

Event samples for signal models involving gluino or squark pair production, in association with up to two additional partons, are generated at leading order with MADGRAPH 5 aMC@NLO, and the decay of the sparticles is performed with PYTHIA 8.2 [53]. Inclusive, process-dependent, signal production cross sections are calculated with NLO plus next-to-leading-logarithm (NLL) accuracy [54–59]. The detector response for signal models is provided by the CMS fast simulation package [60].

The NNPDF3.0 LO and NNPDF3.0 NLO [61] parton distribution functions (PDF) are used, respectively, with the LO and NLO generators described above. The LO PYTHIA 8.2 [53] program is used to describe parton showering and hadronisation for all simulated samples. To model the effects of multiple pp collisions within the same or neighboring bunch crossings (pileup), all simulated events are generated with a nominal distribution of pp interactions per bunch crossing and then reweighted to match the pileup distribution as measured in data. Finally, (near-unity) corrections to the normalisation of the simulated samples for the γ +jets, $W(\rightarrow \mu\nu)$ +jets, $t\bar{t}$, and $Z(\rightarrow \mu\mu)$ +jets, and, equivalently, $Z(\rightarrow \nu\bar{\nu})$ +jets processes are derived using a data sideband to the control regions.

4 Event reconstruction

Global event reconstruction is provided by the particle-flow (PF) algorithm [62, 63], which aims to identify each single particle using an optimized combination of information from all detector systems. In this process, the identification of the particle type (photon, electron, muon, charged hadron, neutral hadron) plays an important rôle in the determination of the particle direction and energy.

The primary vertex (PV) for each recorded event is assumed to be the reconstructed vertex with the largest sum of charged-track p_T^2 values that is found within 24 cm and 2 cm of the center of the detector in the directions along and perpendicular to the beam axis, respectively. Charged tracks associated to reconstructed vertices coincident with the beam axis from other pp interactions within the same or neighbouring bunch crossings (“pileup”) are not considered by the PF algorithm as part of the global event reconstruction.

Photons [64] are identified as ECAL energy clusters not linked to the extrapolation of any charged particle track to the ECAL. The energy of photons is directly obtained from the ECAL measurement, corrected for the effects of pileup. Electrons [65] are identified as a charged particle track associated with an ECAL cluster compatible with the track trajectory, as well as additional ECAL energy clusters from potential bremsstrahlung photons emitted as the electron traverses material of the silicon tracker. The energy of electrons is determined from a combination of the track momentum at the main interaction vertex, the corresponding ECAL cluster energy, and the energy sum of all bremsstrahlung photons attached to the track. Muons [66] are identified as a track in the silicon tracker consistent with either a track or several hits in the muon system. The energy of muons is obtained from the corresponding track momentum. Charged hadrons are identified as charged particle tracks neither identified as electrons, nor as muons. The energy of charged hadrons is determined from a combination of the track momentum and the corresponding ECAL and HCAL energy, corrected for the response function of the calorimeters to hadronic showers. Neutral hadrons are identified as HCAL energy clusters not linked to any charged hadron trajectory, or as ECAL and HCAL energy excesses with respect to the expected charged hadron energy deposit. The energy of neutral hadrons is obtained from the corresponding corrected ECAL and HCAL energy.

Various quality-related criteria must be satisfied in order to identify photons with high efficiency while minimising the misidentification of electrons and associated bremsstrahlung, jets, or ECAL noise as photons. The criteria include the following: the shower shape of the energy deposition in the ECAL must be consistent with that expected from a photon, the energy detected in the HCAL behind the photon shower must not exceed 5% of the photon energy, and no matched hits in the pixel tracker must be found. Similar criteria related to the ECAL shower shape and the relative contributions to the total energy deposited in the ECAL and HCAL must be satisfied to identify electrons, with additional requirements on the associated track that con-

sider the track quality, energy-momentum matching, and compatibility with the PV in terms of the transverse and longitudinal impact parameters.

Photons are required to be isolated from other activity in the event, such as charged and neutral hadrons, within a cone $\Delta R = \sqrt{(\Delta\phi)^2 + (\Delta\eta)^2} = 0.3$ around the photon trajectory, corrected for pileup effects and for contributions from the photon itself. Electrons and muons are also required to be isolated from other activity in the event, primarily to suppress background contributions from semileptonic heavy flavour decays in multijet events. The isolation $I_{\text{rel}}^{\text{mini}}$ is defined as the scalar p_T sum of all charged and neutral hadrons and photons within a cone around the lepton direction, divided by the lepton p_T . The cone radius is dependent on the lepton p_T , primarily to identify with high efficiency the collimated daughter particles of semileptonically decaying Lorentz-boosted top quarks, according to the following: $R = 0.2$ and 0.05 for, respectively, $p_T < 50 \text{ GeV}$ and $p_T > 200 \text{ GeV}$, and $R = 10 \text{ GeV}/p_T$ for $50 < p_T < 200 \text{ GeV}$. The variable $I_{\text{rel}}^{\text{mini}}$ excludes contributions from the lepton itself and is corrected for the effects of pileup. The isolation for electrons and muons is required to satisfy, respectively, $I_{\text{rel}}^{\text{mini}} < 0.1$ and 0.2 for the signal region and nonleptonic control sample selections. A tighter definition of muon isolation, I_{rel}^{μ} , is used when events are required to contain at least one muon. The variable I_{rel}^{μ} is determined identically to $I_{\text{rel}}^{\text{mini}}$ except that a cone of fixed radius $R = 0.4$ is assumed.

Electron and muon candidates identified by the PF algorithm that do not satisfy the quality criteria or the $I_{\text{rel}}^{\text{mini}}$ isolation requirements described above, as well as charged hadrons, are collectively labeled as “single isolated tracks” if they are isolated from neighbouring charged tracks associated to the PV. The isolation $I_{\text{rel}}^{\text{track}}$ is defined as the scalar p_T sum of charged tracks (excluding the track under consideration) within a cone $\Delta R < 0.3$ around the track direction, divided by the track p_T . The requirement $I_{\text{rel}}^{\text{track}} < 0.1$ is imposed.

Jets are clustered from the PF candidate particles with the infrared and collinear safe anti- k_t algorithm [67], operated with a radius parameter R of 0.4 . The jet momentum is determined as the vectorial sum of all particle momenta in this jet, and is found in the simulation to be within 5 to 10% of its true momentum over the whole p_T spectrum and detector acceptance. Jet energy corrections, to account for pileup [68] and to establish a uniform relative response in η and a calibrated absolute response in p_T , are derived from the simulation, and are confirmed with in situ measurements with the energy balance of dijet and photon+jet events [69]. The jet energy resolution amounts typically to 15% at 10 GeV , 8% at 100 GeV , and 4% at 1 TeV , to be compared to about 40%, 12%, and 5% obtained when the calorimeters alone are used for jet clustering. All jets are required to satisfy loose requirements on the relative composition of their particle constituents to reject noise in the calorimeter systems or failures in event reconstruction.

Jets are identified as originating from b quarks using the combined secondary vertex algorithm [70]. Control regions in data [71] are used to measure the probability to correctly identify jets as originating from b quarks (the b-tagging efficiency), the probability to misidentify jets originating from light-flavour partons (u, d, s quarks or gluons) or a charm quark as a b-tagged jet (the light-flavour and charm mistag probabilities). A working point is employed that yields a b-tagging efficiency of 65%, and charm and light-flavour mistag probabilities of, respectively, approximately 12% and 1%, for jets with transverse momenta typical of $t\bar{t}$ events.

5 Event selections

The kinematic selection criteria used to define the signal region, containing a sample of candidate signal events, as well as a number of control regions in data, are described below. The criteria are based on the physics objects defined by the event reconstruction algorithms de-

scribed in Section 4.

5.1 Common preselection criteria

A number of beam and detector related effects, such as beam halo, reconstruction failures, spurious detector noise, or event misreconstruction due to detector inefficiencies, can lead to events with anomolous levels of activity. These events, which can exhibit large, non-physical values of E_T^{miss} , are rejected with high efficiency by applying a range of dedicated vetoes [72–74].

In order to suppress SM processes with genuine E_T^{miss} from neutrinos, events containing an isolated electron or muon that satisfy $p_T > 10 \text{ GeV}$ and $|\eta| < 2.5$ are vetoed. Events containing an isolated photon with $p_T > 25 \text{ GeV}$ and $|\eta| < 2.5$ are also vetoed, in order to select only multijet final states. Furthermore, events containing a single isolated track satisfying $p_T > 10 \text{ GeV}$ and $|\eta| < 2.5$ are vetoed in order to reduce the background contribution from final states containing hadronically-decaying tau leptons.

Each jet j_i is required to satisfy $p_T^{j_i} > 40 \text{ GeV}$ and $|\eta^{j_i}| < 3$. The highest p_T jet in the event is required to have $p_T^{j_1} > 100 \text{ GeV}$ and $|\eta^{j_1}| < 2.5$. The second highest p_T jet in the event is used to categorise events, as described in Section 5.2. If the jet satisfies $p_T^{j_2} > 100 \text{ GeV}$, then this category of events is labelled “symmetric” and targets primarily topologies resulting from pair-produced sparticles. If the jet satisfies $40 < p_T^{j_2} < 100 \text{ GeV}$ or $p_T^{j_2} < 40 \text{ GeV}$, then these categories are labelled as, respectively, “asymmetric” or “monojet” topologies, which target models involving the direct production of stable, weakly interacting, massive particles.

The mass scale of the physics processes being probed is characterised by the scalar p_T sum of the jets, defined as $H_T = \sum_{i=1}^{n_{\text{jet}}} p_T^{j_i}$, where n_{jet} is the number of jets within the experimental acceptance. The magnitude of the negative vector \vec{p}_T sum of these jets, defined by $H_T^{\text{miss}} = |-\sum_{i=1}^{n_{\text{jet}}} \vec{p}_T^{j_i}|$, is used to identify events with a significant imbalance in transverse momentum. Events are vetoed if any jet satisfies $p_T > 40 \text{ GeV}$ and $|\eta| > 3$ to ensure that jets reconstructed in the forward regions of the detector do not contribute significantly to H_T^{miss} .

An estimator of \vec{p}_T^{miss} is given by the projection on the plane perpendicular to the beams of the negative vector sum of the momenta of all candidate particles in an event [74], as determined by the PF algorithm. Its magnitude is referred to as E_T^{miss} . The dimensionless variable $H_T^{\text{miss}}/E_T^{\text{miss}}$ is used to remove events that contain several jets with transverse momenta below the jet p_T thresholds but an appreciable p_T vector sum so as to contribute significantly to H_T^{miss} relative to E_T^{miss} . This background is typical of multijet events, which is suppressed by requiring $H_T^{\text{miss}}/E_T^{\text{miss}} < 1.25$. The requirement is imposed as part of the common preselection criteria used to define all control samples, to minimise potential systematic biases associated with the simulation modelling for this variable. A high efficiency is maintained for SM or new-physics processes that produce unobserved particles, which are characterised by large values of \vec{p}_T^{miss} and values of $H_T^{\text{miss}}/E_T^{\text{miss}}$ close to unity.

Significant jet activity and missing transverse momentum in the event is ensured by requiring $H_T > 200 \text{ GeV}$ and $H_T^{\text{miss}} > 130 \text{ GeV}$, respectively. These requirements complete the common preselection criteria, summarised in Table 1, used to define a sample of all-jet events characterised by high activity and appreciable missing transverse momentum.

5.2 Event categorisation

Events selected by the common preselection criteria are categorised according to n_{jet} , the number of b-tagged jets n_b , and H_T . Nine categories in n_{jet} are employed: the monojet topology

Table 1: Summary of the event selection criteria and categorisation used to define the signal and control regions.

Common preselection	
E_T^{miss} cleaning	Filters related to beam and instrumental effects
Lepton/photon vetoes	$p_T > 10, 10, 25 \text{ GeV}$ for isolated tracks, leptons, photons (respectively) and $ \eta < 2.5$
Jet j_1 acceptance	Consider each jet j_i that satisfies $p_T^{j_i} > 40 \text{ GeV}$ and $ \eta^{j_i} < 3$
Jet j_1 acceptance	$p_T^{j_1} > 100 \text{ GeV}$ and $ \eta^{j_1} < 2.5$
Jet j_2 acceptance	$p_T^{j_2} < 40 \text{ GeV}$ (monojet), $40 < p_T^{j_2} < 100 \text{ GeV}$ (asymmetric), $p_T^{j_2} > 100 \text{ GeV}$ (symmetric)
Forward jet veto	Veto events containing jet satisfying $p_T > 40 \text{ GeV}$ and $ \eta > 3$
Jets below threshold	$H_T^{\text{miss}} / E_T^{\text{miss}} < 1.25$
Energy sums	$H_T > 200 \text{ GeV}$ and $H_T^{\text{miss}} > 130 \text{ GeV}$
Event categorisation	
n_{jet}	1 (monojet), 2, 3, 4, ≥ 5 (asymmetric), 2, 3, 4, ≥ 5 (symmetric)
n_b	0, 1, 2, ≥ 3 ($n_b \leq n_{\text{jet}}$)
H_T (GeV)	200, 250, 300, 350, 400, 500, 600, $> 800 \text{ GeV}$ (bins can be dropped/merged vs. n_{jet} , Table 2)
Signal region (SR)	
QCD multijet rejection	$\alpha_T > 0.65, 0.60, 0.55, 0.53, 0.52, 0.52, 0.52$ (mapped to H_T bins in range $200 < H_T < 800 \text{ GeV}$)
QCD multijet rejection	$\Delta\phi_{\text{min}}^* > 0.5$ (for the region $H_T > 200 \text{ GeV}$)
Control regions (CR)	
Multijet-enriched	SR + $H_T^{\text{miss}} / E_T^{\text{miss}} > 1.25$ (inverted)
γ +jets	1 γ with $p_T > 200 \text{ GeV}$, $ \eta < 1.45$, $\Delta R(\gamma, j_i) > 1.0$, $H_T > 400 \text{ GeV}$, same α_T req. as SR
μ +jets	1 μ with $p_T > 30 \text{ GeV}$, $ \eta < 2.1$, $I_{\text{rel}}^\mu < 0.1$, $\Delta R(\mu, j_i) > 0.5$, $30 < m_T(\vec{p}_T^\mu, \vec{p}_T^{\text{miss}}) < 125 \text{ GeV}$
$\mu^\pm \mu^\mp$ +jets	2 μ with $p_T > 30 \text{ GeV}$, $ \eta < 2.1$, $I_{\text{rel}}^\mu < 0.1$, $\Delta R(\mu_{1,2}, j_i) > 0.5$, $ m_{\mu\mu} - m_Z < 25 \text{ GeV}$

($n_{\text{jet}} = 1$) and four n_{jet} bins (2, 3, 4, ≥ 5) for each of the asymmetric and symmetric topologies. Events are also categorised by n_b (0, 1, 2, ≥ 3), where n_b is bounded from above by n_{jet} , resulting in 32 categories in terms of both n_{jet} and n_b . For each (n_{jet}, n_b) category, events are binned according to H_T : four 50 GeV bins at low jet activity in the range $200 < H_T < 400 \text{ GeV}$, two 100 GeV bins in the range $400 < H_T < 600 \text{ GeV}$, one bin covering the region $600 < H_T < 800 \text{ GeV}$, and a final open bin for $H_T > 800 \text{ GeV}$. These categorisations are summarised in Table 1. The H_T binning scheme is adapted independently per (n_{jet}, n_b) category by removing or merging bins to satisfy a threshold on the minimum number of data events in the control regions, which are used to estimate SM backgrounds, provide checks, and validate assumptions within the methods. The lower bounds of the first and final (open) bins in H_T are summarised in Table 2. In summary, the search employs a categorisation scheme for events that results in 191 bins, defined in terms of n_{jet} , n_b , and H_T .

5.3 Signal region

For events satisfying the common preselection criteria described above, the multijet background dominates over all other SM backgrounds. Several variables are employed to reduce the multijet contribution to a negligible level with respect to other SM backgrounds.

The dimensionless kinematic variable α_T [27, 42], defined in Equ. 2, is used to provide discrimination against multijet events that do not contain significant \vec{p}_T^{miss} or that contain large \vec{p}_T^{miss} only because of transverse momentum mismeasurements, while retaining sensitivity to new-physics events with significant \vec{p}_T^{miss} . The α_T variable depends solely on the transverse component of jet four-momenta and is intrinsically robust against the presence of jet energy mismeasurements in multijet systems. For events containing only two jets, α_T is defined as $\alpha_T = E_T^{j_2} / M_T$, where $E_T = E \sin \theta$, with E the energy of the jet and θ its polar angle with re-

Table 2: Summary of the lower bounds of the first and final bins in H_T (the latter in parentheses) as a function of n_{jet} and n_b .

$n_{\text{jet}} \setminus n_b$	0	1	2	≥ 3
Monojet				
1	200 (600)	200 (500)	-	-
Asymmetric				
2	200 (600)	200 (500)	200 (400)	-
3	200 (600)	200 (600)	200 (500)	200 (300)
4	200 (600)	200 (600)	200 (600)	250 (400)
≥ 5	250 (600)	250 (600)	250 (600)	300 (500)
Symmetric				
2	200 (800)	200 (800)	200 (600)	-
3	200 (800)	250 (800)	250 (800)	- (250)
4	300 (800)	300 (800)	300 (800)	300 (800)
≥ 5	350 (800)	350 (800)	350 (800)	350 (800)

spect to the beam axis, $E_T^{j_2}$ is the transverse energy of the jet with smaller E_T , and M_T is the transverse mass of the dijet system, defined as:

$$M_T = \sqrt{\left(\sum_{i=1}^2 E_T^{j_i}\right)^2 - \left(\sum_{i=1}^2 p_x^{j_i}\right)^2 - \left(\sum_{i=1}^2 p_y^{j_i}\right)^2}, \quad (1)$$

where $E_T^{j_i}$, $p_x^{j_i}$, and $p_y^{j_i}$ are, respectively, the transverse energy and x or y components of the transverse momentum of jet j_i .

For a perfectly measured dijet event with $E_T^{j_1} = E_T^{j_2}$ and the jets in the back-to-back configuration ($\Delta\phi = \pi$), and in the limit in which the momentum of each jet is large compared with its mass, the value of α_T is 0.5. For an imbalance in the E_T of back-to-back jets, α_T is reduced to a value < 0.5 , which gives the variable its intrinsic robustness. Values significantly greater than 0.5 are observed when the two jets are not back-to-back and recoil against \vec{p}_T^{miss} from weakly interacting particles that escape the detector.

The definition of the α_T variable can be generalised for events with more than two jets [27]. The mass scale for any process is characterised through the scalar sum of the jet transverse energies, defined as $\mathcal{H}_T = \sum_{i=1}^{N_{\text{jet}}} |\vec{E}_T^{j_i}|$, where N_{jet} is the number of jets with E_T above a predefined threshold.¹ For events with three or more jets, a pseudo-dijet system is formed by combining the jets in the event into two pseudo-jets. The \mathcal{H}_T for each of the two pseudo-jets is given by the scalar E_T sum of its contributing jets. The combination chosen is the one that minimises $\Delta\mathcal{H}_T$, defined as the difference between these sums for the two pseudo-jets. This clustering criterion assumes a balanced-event hypothesis, which provides strong separation between SM multijet events and events with genuine \vec{p}_T^{miss} . The α_T definition can be generalised to:

$$\alpha_T = \frac{1}{2} \frac{\mathcal{H}_T - \Delta\mathcal{H}_T}{\sqrt{(\mathcal{H}_T)^2 - (H_T^{\text{miss}})^2}}. \quad (2)$$

When jet energies are mismeasured, or there are neutrinos from heavy-flavour quark decays, the magnitude of H_T^{miss} and $\Delta\mathcal{H}_T$ are highly correlated. This correlation is much weaker for

¹The definition of \mathcal{H}_T should be contrasted with that of H_T , the scalar sum of the jet transverse momenta.

R-parity-conserving SUSY events, where each of the two decay chains produces an undetected LSP.

Multijet events populate the region $\alpha_T < 0.5$ and the α_T distribution is characterised by a sharp edge at 0.5, beyond which the multijet event yield falls by several orders of magnitude. Multijet events with extremely rare but large stochastic fluctuations in the calorimetric measurements of jet energies can lead to values of α_T slightly above 0.5. The edge at 0.5 sharpens with increasing H_T for multijet events, primarily due to a corresponding increase in the average jet energy and a consequent improvement in jet energy resolution.

For events containing at least two jets, thresholds on the minimum allowed α_T values are applied independent of n_{jet} and n_b but dependent on H_T , for events that satisfy $200 < H_T < 800$ GeV. The α_T thresholds vary between 0.65 to 0.52 for, respectively, the regions $200 < H_T < 250$ GeV and $400 < H_T < 800$ GeV. No requirement on α_T is made for the region $H_T > 800$ GeV. The thresholds employed are summarised in Table 1. The α_T thresholds are motivated both by the trigger conditions used to record the candidate signal events, described below, and by simulation-based studies and data-derived estimates of the multijet background.

An additional variable is based on the minimum azimuthal separation between a jet and the negative vector \vec{p}_T sum derived from all other jets in the event [27],

$$\Delta\phi_{\min}^* = \min_{\forall j_k \in n_{\text{jet}}} \Delta\phi(-\vec{p}_T^{j_k}, \sum_{\substack{j_i=1 \\ j_i \neq j_k}}^{n_{\text{jet}}} \vec{p}_T^{j_i}). \quad (3)$$

This variable discriminates between final states with genuine \vec{p}_T^{miss} , e.g. from the leptonic decay of the W boson, and energetic multijet events that have significant \vec{p}_T^{miss} through jet energy mismeasurements or through the production of neutrinos, collinear with the axis of a jet, from semileptonic heavy-flavour decays. Multijet events populate the region $\Delta\phi_{\min}^* < 0.5$, with the multijet distribution peaking at a value of zero and falling approximately exponentially over five orders of magnitude to the event level at a value of $\Delta\phi_{\min}^* \approx 0.5$, which is close to the radius parameter value of 0.4 used by the anti- k_t jet clustering algorithm. Events with a genuine source of \vec{p}_T^{miss} exhibit a long tail in $\Delta\phi_{\min}^*$ with values as large as π . The $\Delta\phi_{\min}^*$ variable provides comparable or improved performance in terms of discrimination according to a simple signal-to-background metric for a wide range of signal models with respect to more widely used variables such as:

$$\Delta\phi_{\min} = \min_{\forall j_k \in n_{\text{jet}}} \Delta\phi(\vec{p}_T^{j_k}, -\sum_{j_i=1}^{n_{\text{jet}}} \vec{p}_T^{j_i}). \quad (4)$$

A requirement of $\Delta\phi_{\min}^* > 0.5$ is sufficient to effectively suppress the multijet background to a negligible level while maintaining high efficiency to new-physics signatures. The combined rejection power of the α_T and $\Delta\phi_{\min}^*$ requirements for the region $200 < H_T < 800$ GeV are sufficient to suppress multijet events to the few percent level with respect to all other SM backgrounds in all H_T bins for all event categories of the signal region. For the region $H_T > 800$ GeV, a similar control of the multijet background is achieved solely with the $\Delta\phi_{\min}^* > 0.5$ requirement.

Figure 1 illustrates the performance of the α_T and $\Delta\phi_{\min}^*$ variables, by showing their distributions observed in data for events that satisfy all other signal region selection criteria, as defined

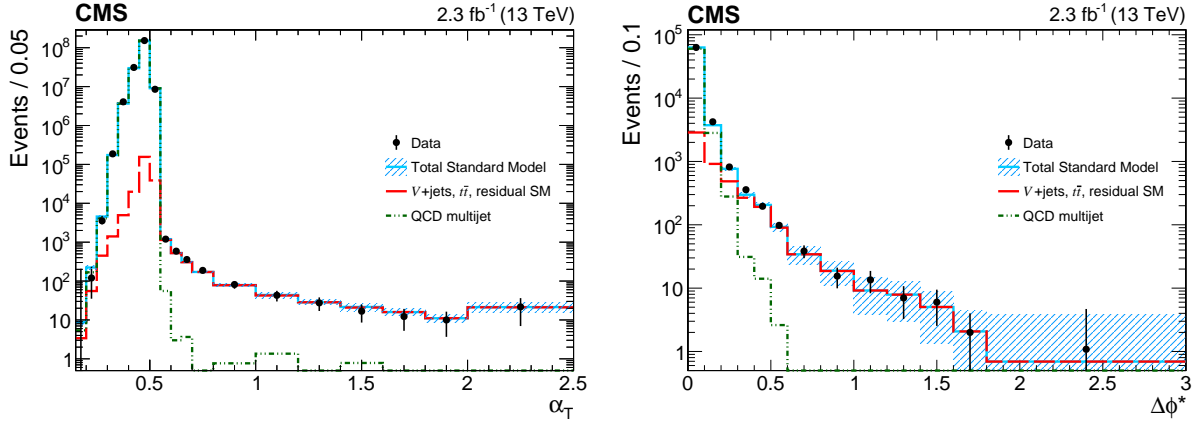


Figure 1: (Left) The α_T distribution observed in data for events that are recorded with an inclusive set of trigger conditions and satisfy either the common preselection criteria and $\alpha_T < 0.55$, or the full signal region selection criteria and $\alpha_T > 0.55$, as well as the additional requirement $H_T > 300$ GeV. (Right) The $\Delta\phi_{\min}^*$ distribution observed in data for events that are recorded with an inclusive set of trigger conditions and satisfy the full signal region selection criteria for the region $H_T > 800$ GeV. The distributions for the QCD multijet backgrounds are determined from simulation while all other SM backgrounds (vector boson production in association with jets, $t\bar{t}$, and other residual contributions from rare SM processes) are estimated using a μ +jets data control sample. These distributions illustrate the performance of these two variables in a kinematic phase space that is representative of the signal region. The statistical uncertainties for the multijet and SM expectations are represented by the hatched areas (visible only for statistically limited bins). The final bin of each distribution contains the overflow events.

in Table 1, and additional requirements on H_T . In the case of the α_T distribution, the events that satisfy $\alpha_T < 0.55$ must only fulfil the common preselection criteria defined in Table 1, no H_T^{miss} requirement is made, and the events are recorded with an inclusive set of trigger H_T conditions that are independent of the α_T variable. In the case of the $\Delta\phi_{\min}^*$ distribution, events are also recorded with an inclusive set of trigger conditions, and must satisfy the full signal region selection criteria for the region $H_T > 800$ GeV. The contribution from multijet events is observed to fall by five orders of magnitude for both variables.

The aforementioned requirements complete the event selection criteria for the signal region. The α_T and $\Delta\phi_{\min}^*$ requirements, in conjunction with the common preselection requirements $H_T^{\text{miss}} > 130$ GeV and $H_T^{\text{miss}}/E_T^{\text{miss}} < 1.25$, provide strong rejection power against contributions from multijet events. Finally, a modification to the $\Delta\phi_{\min}^*$ variable, which considers soft jets with $p_T > 25$ GeV and is henceforth labeled $\Delta\phi_{\min}^{*25}$, is used as a control variable in data to identify multijet contributions arising from instrumental effects, such as inefficient detector elements or detector noise. The axis of any jet that satisfies $\Delta\phi_{\min}^{*25} < 0.5$ is used to identify localised behaviour in the (η, ϕ) plane, which may be indicative of instrumental defects. No significant anomalies are observed in the sample of candidate signal events following the application of the dedicated vetoes mentioned in Section 5.1.

Multiple trigger conditions are employed in combination to record signal candidate events. A set of trigger conditions utilise calculations of both H_T and α_T to record events with two or more jets. An event is recorded if it satisfies any of the following pairs of (H_T, α_T) thresholds, (200,0.57), (250,0.55), (300,0.53), (350,0.52), or (400,0.51), as well as a requirement on the mean value of the two highest p_T jets, $\langle p_T^{j_1} + p_T^{j_2} \rangle > 90$ GeV. These requirements are collectively labelled as the “ H_T - α_T ” triggers. In addition, candidate signal events with one or more jets

are also recorded if they satisfy the requirements $H_T^{\text{miss}} > 90 \text{ GeV}$ and $E_T^{\text{miss}} > 90 \text{ GeV}$. Finally, for events that satisfy $H_T > 800 \text{ GeV}$, a further trigger requirement, defined by $H_T > 800 \text{ GeV}$, is employed in addition to the $H_T - \alpha_T$ trigger requirements, to record events characterised by high activity in the calorimeters with high efficiency. The trigger-level jet energies are corrected to account for energy scale and pileup effects. The aforementioned triggers are employed in combination to provide efficiencies at or near 100% for all bins in the signal region.

5.4 H_T^{miss} templates

Following the event selections described above, which provide a sample of signal candidate events with a negligible contribution from multijet events, further discriminating power is required to separate new-physics signatures from the remaining SM backgrounds, which are dominated by the production of $t\bar{t}$ or $W(\rightarrow \ell\nu) + \text{jets}$ and $Z(\rightarrow \nu\bar{\nu}) + \text{jets}$ events. Given the characteristic signature of SUSY production at the LHC is a final state of multijets accompanied by large values of \vec{p}_T^{miss} from the LSPs, the search exploits the use of the H_T^{miss} variable as an additional discriminant between new-physics and SM processes.

The search relies directly on simulation to provide an estimate of the expected distribution of events as a function of H_T^{miss} in each $(n_{\text{jet}}, n_b, H_T)$ bin. The distributions are described by templates that are used by the likelihood function as a model for the data, details on which can be found in Section 7. The templates are extensively validated against data in multiple control regions, and these studies are used to establish the uncertainty in the simulation modelling of the H_T^{miss} variable. The effect of theoretical and experimental uncertainties on the H_T^{miss} distributions are also studied. Further details can be found in Sections 6.2.

5.5 Control regions

Four control regions in data are employed to estimate the background contributions from SM processes, which modify and expand on the common preselection criteria described above, according to the descriptions found below and summarised in Table 1.

The first control region comprises a multijet-enriched sample of events, and is defined by the signal region selection criteria and the inverted requirement $H_T^{\text{miss}}/E_T^{\text{miss}} > 1.25$. The events are recorded with the signal triggers described above, and the sample is used to estimate the multijet background in the signal region.

Three additional control regions are used to estimate background contributions from SM processes with final states containing genuine \vec{p}_T^{miss} , and are defined by inverting one of the photon or lepton vetoes to select samples of $\gamma + \text{jets}$, $\mu + \text{jets}$, or $\mu\mu + \text{jets}$ events. Additional kinematic requirements are employed to ensure the control samples are enriched in the same SM processes that contribute to background events in the signal region, and are depleted in contributions from multijet production or a wide variety of SUSY models (i.e. so-called signal contamination). The samples are defined, and their events are identically categorised and binned, such that the kinematic properties of events in the control regions and the signal candidate events resemble as closely as possible one another, once the photon, muon, or dimuon system is ignored in the calculation of quantities such as H_T and H_T^{miss} . The selections are summarised in Table 1 and described below.

The $\gamma + \text{jets}$ event sample is defined by the common preselection requirements, but the photon veto is inverted and each event is required to contain a single isolated photon, as defined in Section 4, that satisfies $p_T > 200 \text{ GeV}$ and $|\eta| < 1.45$ and well separated from each jet j_i in the event according to $\Delta R(\gamma, j_i) > 1.0$. In addition, events must satisfy $H_T > 400 \text{ GeV}$, as well as the same H_T -dependent α_T requirements used to define the signal region. The events are

recorded using a single-photon trigger condition and the selections result in a trigger efficiency of $\gtrsim 99\%$.

The μ +jets event sample is defined by the common preselection requirements, but the muon veto is inverted and each event is required to contain a single isolated muon, as defined in Section 4, that satisfies $p_T > 30 \text{ GeV}$ and $|\eta| < 2.1$ and well separated from each jet j_i in the event according to $\Delta R(\mu, j_i) > 0.5$. The transverse mass formed by the transverse momenta of the muon and \vec{p}_T^{miss} system must satisfy $30 < m_T < 125 \text{ GeV}$ to select a sample of events rich in W bosons, produced promptly or from the decay of top quarks. The $\mu\mu$ +jets sample uses a similar set of selection criteria as the μ +jets sample, but specifically requires two oppositely charged isolated muons that both satisfy $p_T > 30 \text{ GeV}$ and $|\eta| < 2.1$ and are well separated from the jets in the event ($\Delta R(\mu_{1,2}, j_i) > 0.5$). The muons are also required to have a dilepton invariant mass within a $\pm 25 \text{ GeV}$ window around the nominal mass of the Z boson. For both the muon and dimuon samples, no requirement is made on α_T , in order to increase the statistical precision of the predictions from these samples. Both the μ +jets and $\mu\mu$ +jets samples are recorded using a trigger that requires an isolated muon. The selection criteria of the μ +jets and $\mu\mu$ +jets event samples are chosen so that the trigger is maximally efficient with values, respectively, in the region of $\sim 90\%$ and $\sim 99\%$.

6 Estimation of backgrounds

6.1 Multijets background

The signal region is defined in a manner to suppress the expected contribution from multijet production to the percent level with respect to the total expected background counts from other SM processes for all event categories, defined in terms of n_{jet} and n_b , and all bins, defined in H_T and H_T^{miss} . This is achieved primarily through the application of very tight requirements on the variables α_T and $\Delta\phi_{\text{min}}^*$, as described in Section 5.3, as well as the requirement $H_T^{\text{miss}}/E_T^{\text{miss}} < 1.25$. In this section, we discuss these requirements further, and the estimate of the suppression of the multijet background.

The contamination from multijet events in the signal region is estimated using a multijet-enriched data sideband to the signal region, defined by the (inverted) requirement $H_T^{\text{miss}}/E_T^{\text{miss}} > 1.25$. The observed counts in data, categorised according to n_{jet} and H_T , are corrected to account for contamination from non-multijet SM processes, and the corrected counts $\mathcal{N}^{\text{data}}(n_{\text{jet}}, H_T)$ are assumed to arise solely from QCD multijet production. The non-multijet processes, which comprise vector boson and $t\bar{t}$ production, and residual contributions from other SM processes, are estimated using the μ +jets control region using the method described in Section 6.2. Independent ratios $\mathcal{R}^{\text{QCD}}(n_{\text{jet}}, H_T)$ of multijet events that satisfy the requirement $H_T^{\text{miss}}/E_T^{\text{miss}} < 1.25$ to those that fail, where the events are categorised according to n_{jet} and H_T , are determined from simulation. The product of a ratio $\mathcal{R}^{\text{QCD}}(n_{\text{jet}}, H_T)$ and a corrected data count $\mathcal{N}^{\text{data}}(n_{\text{jet}}, H_T)$ provides the estimate of the multijet background $\mathcal{P}(n_{\text{jet}}, H_T)$. Each estimate is assumed to distribute identically to the non-multijet backgrounds as a function of n_b and H_T^{miss} . This final assumption, implemented by the multiplier term $\mathcal{K}_{n_{\text{jet}}, H_T}(n_b, H_T^{\text{miss}})$, is based on studies in simulation and is a valid approximation given the magnitude of the uncertainties assumed in the method to estimate this residual background contribution, described below. Assuming i, j, k , and l are the bin indices for, respectively, n_{jet}, H_T, n_b , and H_T^{miss} :

$$\mathcal{P}(i, j, k, l) = \mathcal{N}^{\text{data}}(i, j) \mathcal{R}^{\text{QCD}}(i, j) \mathcal{K}_{i,j}(k, l). \quad (5)$$

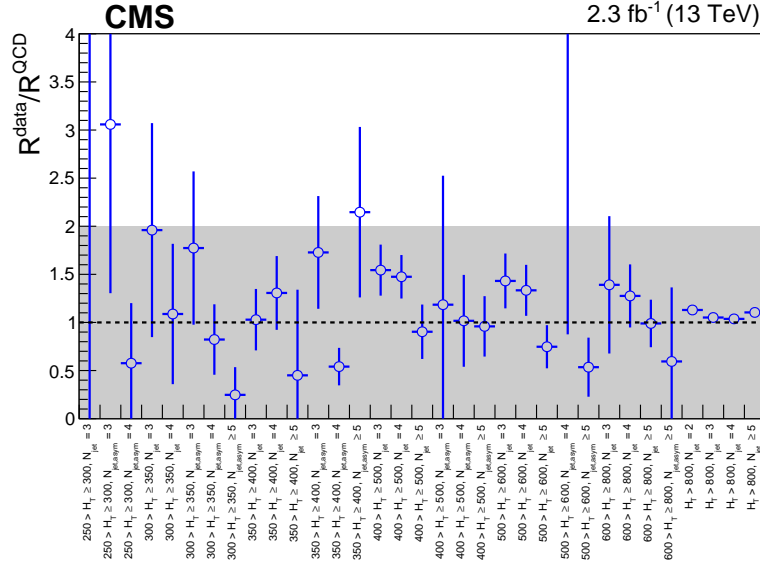


Figure 2: Validation of the ratio \mathcal{R}^{QCD} determined from simulation in bins of n_{jet} and H_T by comparing with an equivalent ratio $\mathcal{R}^{\text{data}}$ constructed from data in a multijet-enriched sideband to the signal region. A value of unity is expected for the double ratio $\mathcal{R}^{\text{data}}/\mathcal{R}^{\text{QCD}}$, and the grey shaded band represents the assumed systematic uncertainty of 100% in \mathcal{R}^{QCD} .

The use of simulation to determine $\mathcal{R}^{\text{QCD}}(n_{\text{jet}}, H_T)$ is validated using a multijet-enriched data sideband defined by $\Delta\phi_{\text{min}}^* < 0.5$. The ratio $\mathcal{R}^{\text{data}}(n_{\text{jet}}, H_T)$ is constructed from data counts, corrected to account for contributions from non-multijet processes, and compared with $\mathcal{R}^{\text{QCD}}(n_{\text{jet}}, H_T)$, determined from simulation, through the double ratio $\mathcal{R}^{\text{data}}/\mathcal{R}^{\text{QCD}}$, as shown in Fig. 2. The double ratios are observed to be close to, or statistically compatible with, unity across the full phase space of the signal region, including the bins at high H_T , which exhibit the highest statistical precision. An uncertainty of 100% in \mathcal{R}^{QCD} is assumed to adequately cover the observed level of agreement for the full signal region phase space, as well as any limitations in the assumptions on the distribution of multijet events as a function of n_b and H_T^{miss} for all regions defined in terms of n_{jet} and H_T .

6.2 Backgrounds with genuine E_T^{miss}

Following the suppression of multijet events through the use of the α_T and $\Delta\phi_{\text{min}}^*$ variables, the dominant non-multijet backgrounds involve SM processes that produce high- p_T neutrinos in the final state. In events with few jets or few b quark jets, the associated production of W or Z bosons and jets, with the decays $W^\pm \rightarrow \ell\nu$ ($\ell = e, \mu, \tau$) or $Z \rightarrow \nu\bar{\nu}$, dominate the background counts. For W boson decays that yield a muon or electron (possibly originating from leptonic τ decays), the background arises when the event containing the μ or e is not rejected by the lepton vetoes. Background also arises when the τ lepton decays to hadrons, identified as a jet, and neutrinos. The veto of events containing at least one isolated track is efficient at further suppressing these backgrounds, including those from single-prong τ -lepton decays. At higher jet or b quark jet multiplicities, single top and $t\bar{t}$ production, followed by semileptonic top quark decay, also become an important source of background.

The method to estimate the non-multijet backgrounds in the signal region relies on the use of a transfer (\mathcal{T}) factor determined from simulation that is constructed per bin (in terms of n_{jet} , n_b , and H_T) per control region. Each \mathcal{T} factor is defined as the ratio of the expected yields

in the same $(n_{\text{jet}}, n_b, H_T)$ bins of the signal region $\mathcal{N}_{\text{MC}}^{\text{SR}}$ and one of the control regions $\mathcal{N}_{\text{MC}}^{\text{CR}}$. The \mathcal{T} factors are used to extrapolate from the event yields observed in each bin of a data control sample $\mathcal{N}_{\text{data}}^{\text{CR}}$ to provide an estimate for the background, integrated over H_T^{miss} , from a particular SM process or processes in the corresponding bin of the signal region $\mathcal{N}_{\text{data}}^{\text{SR}}$. The superscript SR or CR refers to, respectively, the process or processes being estimated and one of the μ +jets, $\mu\mu$ +jets, and γ +jets control regions, described in Section 5.5. The subscript refers to whether the counts are obtained from data, simulation (“MC”) or an estimate (“pred”).

The method aims to minimise the effects of simulation mismodelling, as many systematic biases in the simulation are expected to largely cancel in the \mathcal{T} factors, given that the events in any given $(n_{\text{jet}}, n_b, H_T)$ bin of the control regions closely mirror those in the corresponding bin in the signal region, in terms of the event scale and topology, the kinematic phase, and the relative background compositions. In short, minimal extrapolations are made. Uncertainties in the \mathcal{T} factors are determined from a data-derived approach, described below.

Three independent estimates of the irreducible background of $Z \rightarrow \nu\bar{\nu}$ + jets events are determined from the γ +jets, $\mu\mu$ +jets, and μ +jets data control samples. The γ +jets and $Z \rightarrow \mu\mu$ + jets processes have similar kinematic properties when the photon or muons are ignored [75], albeit different acceptances. In addition, the γ +jets process has a larger production cross section than $Z \rightarrow \nu\bar{\nu}$ + jets events. The μ +jets data sample is used to provide an estimate for both the $Z \rightarrow \nu\bar{\nu}$ + jets background, as well as the other dominant SM processes, $t\bar{t}$ and W boson production (labelled collectively as $W/t\bar{t}$). Residual contributions from all other SM relevant processes, such as single-top-quark, diboson, and Drell-Yan production, are also included as part of the $W/t\bar{t}$ estimate from the μ +jets sample. The definition of the various \mathcal{T} factors used in the search are given below:

$$\mathcal{N}_{\text{pred}}^{W/t\bar{t}} = \mathcal{T}_{\mu\text{+jets}}^{W/t\bar{t}} \mathcal{N}_{\text{data}}^{\mu\text{+jets}}, \quad \mathcal{T}_{\mu\text{+jets}}^{W/t\bar{t}} = \left(\frac{\mathcal{N}_{\text{MC}}^{W/t\bar{t}}}{\mathcal{N}_{\text{MC}}^{\mu\text{+jets}}} \right) \quad (6)$$

$$\mathcal{N}_{\text{pred}}^{Z \rightarrow \nu\bar{\nu}} = \mathcal{T}_{\mu\text{+jets}}^{Z \rightarrow \nu\bar{\nu}} \mathcal{N}_{\text{data}}^{\mu\text{+jets}}, \quad \mathcal{T}_{\mu\text{+jets}}^{Z \rightarrow \nu\bar{\nu}} = \left(\frac{\mathcal{N}_{\text{MC}}^{Z \rightarrow \nu\bar{\nu}}}{\mathcal{N}_{\text{MC}}^{\mu\text{+jets}}} \right) \quad (7)$$

$$\mathcal{N}_{\text{pred}}^{Z \rightarrow \nu\bar{\nu}} = \mathcal{T}_{\mu\mu\text{+jets}}^{Z \rightarrow \nu\bar{\nu}} \mathcal{N}_{\text{data}}^{\mu\mu\text{+jets}}, \quad \mathcal{T}_{\mu\mu\text{+jets}}^{Z \rightarrow \nu\bar{\nu}} = \left(\frac{\mathcal{N}_{\text{MC}}^{Z \rightarrow \nu\bar{\nu}}}{\mathcal{N}_{\text{MC}}^{\mu\mu\text{+jets}}} \right) \quad (8)$$

$$\mathcal{N}_{\text{pred}}^{Z \rightarrow \nu\bar{\nu}} = \mathcal{T}_{\gamma\text{+jets}}^{Z \rightarrow \nu\bar{\nu}} \mathcal{N}_{\text{data}}^{\gamma\text{+jets}}, \quad \mathcal{T}_{\gamma\text{+jets}}^{Z \rightarrow \nu\bar{\nu}} = \left(\frac{\mathcal{N}_{\text{MC}}^{Z \rightarrow \nu\bar{\nu}}}{\mathcal{N}_{\text{MC}}^{\gamma\text{+jets}}} \right) \quad (9)$$

The likelihood function, described in Section 7, encodes the estimate via the \mathcal{T} factors of the $W/t\bar{t}$ background, as well as the three independent estimates of the $Z \rightarrow \nu\bar{\nu}$ background, which are considered simultaneously.

Several sources of uncertainty in the \mathcal{T} factors are evaluated. The most relevant effects are discussed below, and generally fall into one of two categories. The first category concerns uncertainties in “scale factor” corrections applied to simulation, which are determined using inclusive data samples that are defined by loose selection criteria, to account for the mismodelling of theoretical and experimental parameters. The second category concerns “closure tests” in data that probe various aspects of the accuracy of the simulation to model correctly the \mathcal{T} factors in the phase space of this search.

The uncertainties in the \mathcal{T} factors are studied for variations in scale factors related to: the jet

Table 3: Systematic uncertainties (percent) in the transfer factors (\mathcal{T}) used in the method to estimate the SM backgrounds with genuine \vec{p}_T^{miss} in the signal region. The quoted ranges provide representative values of the observed variations as a function of n_{jet} and H_T .

Systematic source	Uncertainty in \mathcal{T} factor [%]			
	$\mathcal{T}_{\mu+\text{jets}}^{W/\text{t}\bar{\text{t}}}$	$\mathcal{T}_{\mu+\text{jets}}^{Z \rightarrow \nu\bar{\nu}}$	$\mathcal{T}_{\mu+\text{jets}}^{Z \rightarrow \mu\bar{\mu}}$	$\mathcal{T}_{\gamma+\text{jets}}^{Z \rightarrow \mu\bar{\mu}}$
<i>Scale factors (applied to simulation):</i>				
Jet energy scale	< 15%	< 15%	< 10%	< 15%
b-tag eff. mistag	< 5%	< 5%	< 2%	< 2%
Lepton SFs	2 – 5%	2 – 5%	2 – 5%	–
Pileup	< 10%	< 6%	< 4%	< 3%
Top quark p_T	< 5%	< 20%	< 4%	–
<i>Closure tests:</i>				
W/Z ratio	–	10 – 30%	–	–
Z/ γ ratio	–	–	–	10 – 30%
W/ $\text{t}\bar{\text{t}}$ composition	10 – 100%	–	–	–
W polarisation	5 – 50%	5 – 50%	–	–
$\alpha_T / \Delta\phi_{\text{min}}^*$	5 – 80%	5 – 80%	50 – 80%	–

energy scale (that result in uncertainties in the \mathcal{T} factors as large as $\sim 15\%$), the efficiency and misidentification probability of b quark jets (up to 5%), and the efficiency to identify well-reconstructed, isolated leptons (up to $\sim 5\%$). A 5% uncertainty in the minimum bias cross section, $\sigma_{\text{MB}} = 69.0 \pm 3.5 \text{ mb}$, is assumed and propagated through to the reweighting procedure to account for differences between the simulated and data-derived measurements of the pileup distributions, which results in changes of up to $\sim 10\%$. The modelling of the transverse momentum of top quarks (p_T^t) is evaluated by comparing the simulated and measured p_T spectra of reconstructed top objects in $\text{t}\bar{\text{t}}$ events. Simulated events are reweighted according to scale factors that decrease from a value of ~ 1.2 to ~ 0.7 , with uncertainties of ~ 0.1 – 0.2 , within the range $0 < p_T^t < 400 \text{ GeV}$. The systematic uncertainties in the $\mathcal{T}_{\mu+\text{jets}}^{W/\text{t}\bar{\text{t}}}$ factors arising from variations in the p_T^t scale factors are typically small ($\lesssim 5\%$), due to the comparable phase space probed by the signal and control regions, while larger uncertainties ($\lesssim 20\%$) in the $\mathcal{T}_{\mu+\text{jets}}^{Z \rightarrow \nu\bar{\nu}}$ factors are observed, due to the potential for significant contamination from $\text{t}\bar{\text{t}}$ when using $W(\rightarrow \ell\nu) + \text{jets}$ to predict $Z(\rightarrow \nu\bar{\nu}) + \text{jets}$.

The aforementioned systematic uncertainties, resulting from variations in scale factors, are summarised in Table 3, along with representative magnitudes. Each source of uncertainty is assumed to vary with a fully correlated behaviour across the full phase space of the signal and control regions.

The second category of sources of uncertainty are determined from sets of “closure tests” based on data control samples [30]. Each set uses the observed event counts in up to eight bins in H_T for each of the nine n_{jet} event categories in one of the three independent data control regions. These counts are used with the corresponding \mathcal{T} factors, determined from simulation, to obtain a prediction, $\mathcal{N}^{\text{pred}}(n_{\text{jet}}, H_T)$, of the observed yields, $\mathcal{N}^{\text{obs}}(n_{\text{jet}}, H_T)$, in another control sample (or, in one case, n_b event category).

Each set of tests targets a specific (potential) source of bias in the simulation modelling that may introduce an n_{jet} - or H_T -dependent source of systematic bias in the \mathcal{T} factors [30]. Several sets of tests are performed. The Z/ γ ratio determined from simulation is tested against the same ratio measured using $Z(\rightarrow \mu\mu) + \text{jets}$ events and the $\gamma + \text{jets}$ sample. The W/Z ratio is also probed using the $\mu + \text{jets}$ and $\mu\mu + \text{jets}$ samples, which directly tests the simulation modelling of vector

boson production, as well as the modelling of $t\bar{t}$ contamination in the μ +jets sample. A further set probes the modelling of the relative composition between $W(\rightarrow \ell\nu)$ +jets and $t\bar{t}$ events using μ +jets events containing exactly zero or one more b-tagged jets, which represents a larger extrapolation in relative composition than used in the search. The effects of W polarisation are probed by using μ +jets events with a positively charged muon to predict those containing a negatively charged muon. Finally, the accuracy of the modelling of the efficiencies of the α_T and $\Delta\phi_{\min}^*$ requirements are estimated using the μ +jets sample.

For each set of tests, the level of closure, $(\mathcal{N}^{\text{obs}} - \mathcal{N}^{\text{pred}})/\mathcal{N}^{\text{obs}}$, which considers only statistical uncertainties, is inspected to ensure no statistically significant biases are observed as a function of the nine n_{jet} categories or the eight H_T bins. In the absence of such a bias, the level of closure is recomputed by integrating over either all monojet and asymmetric n_{jet} categories, or the symmetric n_{jet} categories. The level of closure and its statistical uncertainty are combined in quadrature to determine additional contributions to the uncertainties in the \mathcal{T} factors. These uncertainties are considered to be fully correlated between the monojet and asymmetric n_{jet} categories or the symmetric n_{jet} categories, and fully uncorrelated between these two regions in n_{jet} and H_T bins. If the closure tests use the $\mu\mu$ +jets sample, the level of closure is determined by additionally integrating over pairs of adjacent H_T bins. These uncertainties, derived from the closure tests in data, are summarised in Table 3, along with representative magnitudes. These uncertainties are the dominant contribution to the total uncertainty in the \mathcal{T} factors, due to the limited number of events in the data control regions.

As introduced in Section 5.4, templates are derived from simulation to predict the background counts in the H_T^{miss} dimension. The uncertainties in the \mathcal{T} factors are used to constrain the normalisation of the H_T^{miss} templates. The uncertainties in the H_T^{miss} shape are discussed below.

The accuracy to which the simulation describes the H_T^{miss} distributions is evaluated with respect to data, in each $(n_{\text{jet}}, n_b, H_T)$ bin in each of the μ +jets, $\mu\mu$ +jets, and γ +jets data control regions. The level of agreement between data and simulation as a function of H_T^{miss} is parameterised using an orthogonal first-order polynomial, $f(x) = p_0 + p_1(\bar{x} - x)$, and described by two uncorrelated parameters, p_0 and p_1 . A binned likelihood fit is performed in each $(n_{\text{jet}}, n_b, H_T)$ bin of each control region, and the best fit value p_1 and its uncertainty is used to determine the presence of biases dependent on H_T^{miss} . The pull of p_1 from a value of zero is defined as the best fit value over its standard deviation, considering only statistical uncertainties associated with the finite size of the data and simulated samples.

The lower bound of the final (open) bin in H_T^{miss} is not more than 800 GeV and is bounded from above by the upper bound of the H_T bin in question. The lower bound of the final H_T^{miss} bin is merged with lower bins if fewer than ten events in the data control regions are observed. If a bin in $(n_{\text{jet}}, n_b, H_T)$ contains fewer than ten events, the H_T^{miss} template is not used. The merging of bins is typically only relevant for event categories that satisfy $n_b \geq 2$.

The presence of systematic biases is evaluated at a statistical level, by considering the distribution of pulls obtained from each control region, which are consistent with statistical fluctuations, with no indication of trends across the full phase space of each control region. The p -values obtained from the fits are uniformly distributed.

The uncertainty in the H_T^{miss} modelling is extracted under the hypothesis of no bias. This is done using the maximum likelihood (ML) values of the fit parameters to determine the statistical precision to which this hypothesis can be confirmed. The quadrature sum of the ML value and its uncertainty for p_1 from each fit is used to define alternative templates that represent $\pm 1\sigma$ variations to the nominal H_T^{miss} template. These alternative templates are encoded in the

likelihood function, as described in Section 7. The observed variations are compatible with the expected values obtained from studies relying only on simulated event samples. The uncertainties in the final H_T^{miss} bin of the templates depend on the event category and H_T bin, but are typically found to be in the range $\sim 10\text{--}100\%$.

The effect on the H_T^{miss} templates is determined under $\pm 1\sigma$ variations in the jet energy scale, the efficiency and misidentification probability of b quark jets, the efficiency to identify well-reconstructed, isolated leptons, the pileup reweighting, and the modelling in the top quark transverse momentum. These effects are easily covered by the data-derived uncertainties, described above, across the full phase space of the control regions, which mirror closely that of the signal region.

7 Results

A model of the observations in all data samples, described by a likelihood function, is used to obtain a prediction of the SM backgrounds, and to test for the presence of new-physics signals if the signal region is included in the maximum-likelihood fit. The observation in each bin defined by the n_{jet} , n_b , H_T , and H_T^{miss} variables is modelled as a Poisson-distributed variable around the SM expectation and a potential signal contribution (assumed to be zero in the following discussion), where the SM expectation is the sum over the estimated contributions from all background processes according to the methods described in Section 6.

The non-multijet backgrounds are related to the expected yields in the $\mu + \text{jets}$, $\mu\mu + \text{jets}$, and $\gamma + \text{jets}$ control samples via the \mathcal{T} factors derived from simulation, as described in Section 5.5. Estimates of the contribution from multijet events in the signal region is determined according to the method described in Section 6.1, and is included in the likelihood function.

The systematic uncertainties summarised in Table 3 are accommodated in the likelihood function through the use of nuisance parameters, the measurements of which are assumed to follow a log-normal distribution. Alternative templates are used to describe the uncertainties in the modelling of the H_T^{miss} variable. A vertical template morphing scheme [76] is used to interpolate between the nominal and alternative H_T^{miss} templates. A nuisance parameter controls the interpolation, which is gaussian distributed with a mean of zero and a standard deviation of one, where ± 1 corresponds to the alternative templates for a $\pm 1\sigma$ variation in the uncertainty. Each template is interpolated quadratically between $\pm 1\sigma$, and a linear extrapolation is employed beyond these bounds.

The “pre-fit” result of this search, which considers the observations in the control regions only, is summarised in Figs. 3, 4, and 5 for, respectively, the monojet, asymmetric, and symmetric topologies. The figures also show the significance of deviations observed in data with respect to the “pre-fit” SM expectations, expressed in terms of the total uncertainty in the SM expectations. Figures 3, 4, and 5 also summarise the pulls from the “post-fit” result, which is based on a maximum-likelihood fit to observations in the signal region as well as the control regions. The data are well described by the background-only hypothesis. A saturated likelihood model is used as a goodness-of-fit test to determine the compatibility of the observed yields with the expectations under the background-only hypothesis. A p -value of 0.20 is observed for the fit over the full signal region, and p -values in the range 0.04–1.00, consistent with a uniform distribution, are obtained when considering events categorised according to n_{jet} . The covariance and correlation matrices for the pre-fit SM expectations in all bins of the signal region, defined by n_{jet} , n_b , H_T , and integrated over H_T^{miss} , are determined from 500 pseudo-experiments by sampling the pre-fit nuisance parameters under the background-only hypothesis. The SM ex-

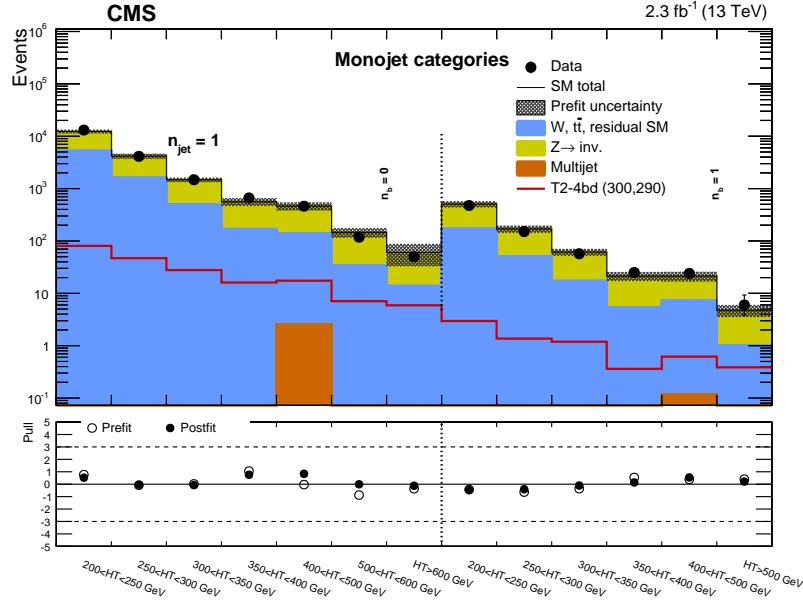


Figure 3: (Top panel) Event yields observed in data (solid circles) and “pre-fit” SM expectations with their associated uncertainties (black histogram with shaded band), integrated over H_T^{miss} , as a function of n_b , and H_T for the monojet category ($n_{\text{jet}} = 1$) in the signal region. For illustration only, the expectations for a benchmark model (T2tt_degen with $m_{\tilde{t}} = 300$ GeV and $m_{\tilde{\chi}_1^0} = 290$ GeV) are superimposed on the SM-only expectations. (Bottom panel). The significance of deviations observed in data with respect to the “pre-fit” (open circles) and “post-fit” (closed circles) SM expectations, expressed in terms of the total uncertainty in the SM expectations.

641 expectations for different n_{jet} and n_b categories exhibit a nonnegligible level of covariance within
 642 the same H_T bin, primarily as a result of the systematic uncertainties evaluated from closure
 643 tests, described in Section 6.2, that integrate yields over n_{jet} and n_b . Bins adjacent and next-
 644 to-adjacent in n_{jet} and/or n_b can have correlation coefficients in the range 0.2–0.4, and, infre-
 645 quently, as large as ~ 0.5 . Otherwise, the correlation coefficients are < 0.2 . Anti-correlation
 646 coefficients are typically not larger than ~ 0.2 .

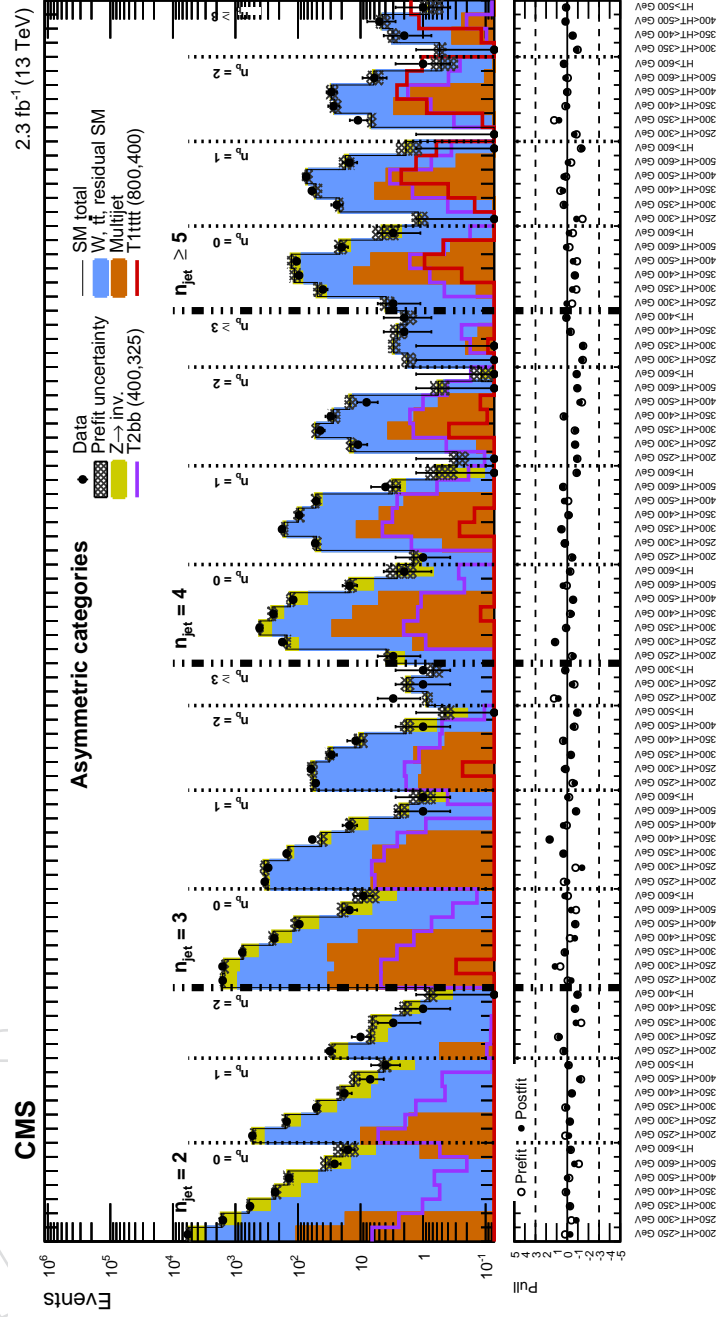


Figure 4: (Top panel) Event yields observed in data (solid circles) and “pre-fit” SM expectations with their associated uncertainties (black histogram with shaded band), integrated over H_T^{miss} , as a function of n_{jet} , n_b , and H_T for the “asymmetric” n_{jet} categories in the signal region. For illustration only, the expectations for two benchmark models (T2bb with $m_{\tilde{b}} = 400$ GeV and $m_{\tilde{\chi}_1^0} = 325$ GeV, T1tttt with $m_{\tilde{g}} = 800$ GeV and $m_{\tilde{\chi}_1^0} = 400$ GeV) are superimposed on the SM-only expectations. (Bottom panel). The significance of deviations observed in data with respect to the “pre-fit” (open circles) and “post-fit” (closed circles) SM expectations, expressed in terms of the total uncertainty in the SM expectations.

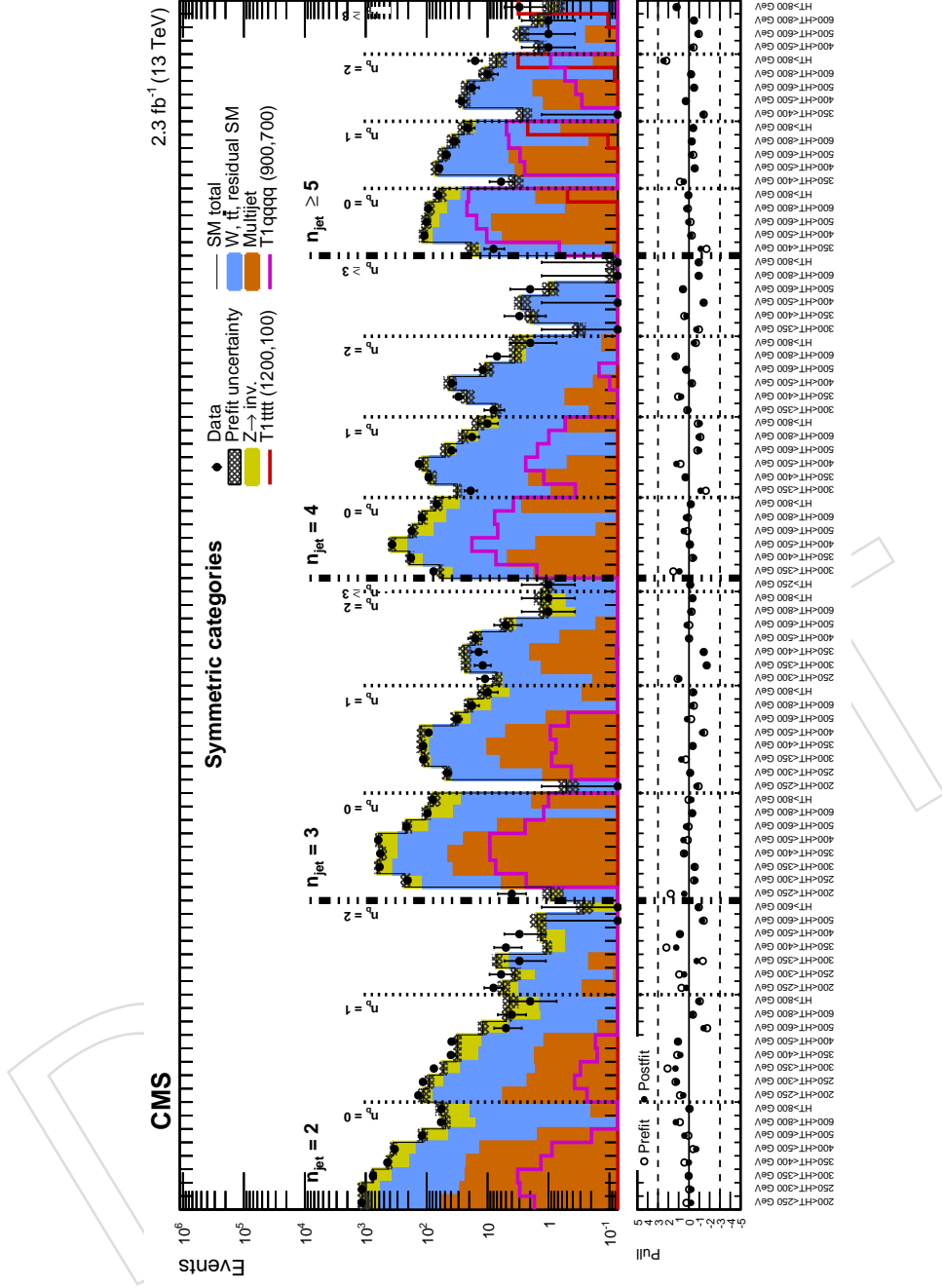


Figure 5: (Top panel) Event yields observed in data (solid circles) and “pre-fit” SM expectations with their associated uncertainties (black histogram with shaded band), integrated over H_T^{miss} , as a function of n_{jet} , n_b , and H_T for the “symmetric” n_{jet} categories in the signal region. For illustration only, the expectations for two benchmark models (T1ttttt with $m_{\tilde{g}} = 1200$ GeV and $m_{\tilde{\chi}_1^0} = 100$ GeV, T1qqqq with $m_{\tilde{g}} = 900$ GeV and $m_{\tilde{\chi}_1^0} = 700$ GeV) are superimposed on the SM-only expectations. (Bottom panel). The significance of deviations observed in data with respect to the “pre-fit” (open circles) and “post-fit” (closed circles) SM expectations, expressed in terms of the total uncertainty in the SM expectations.

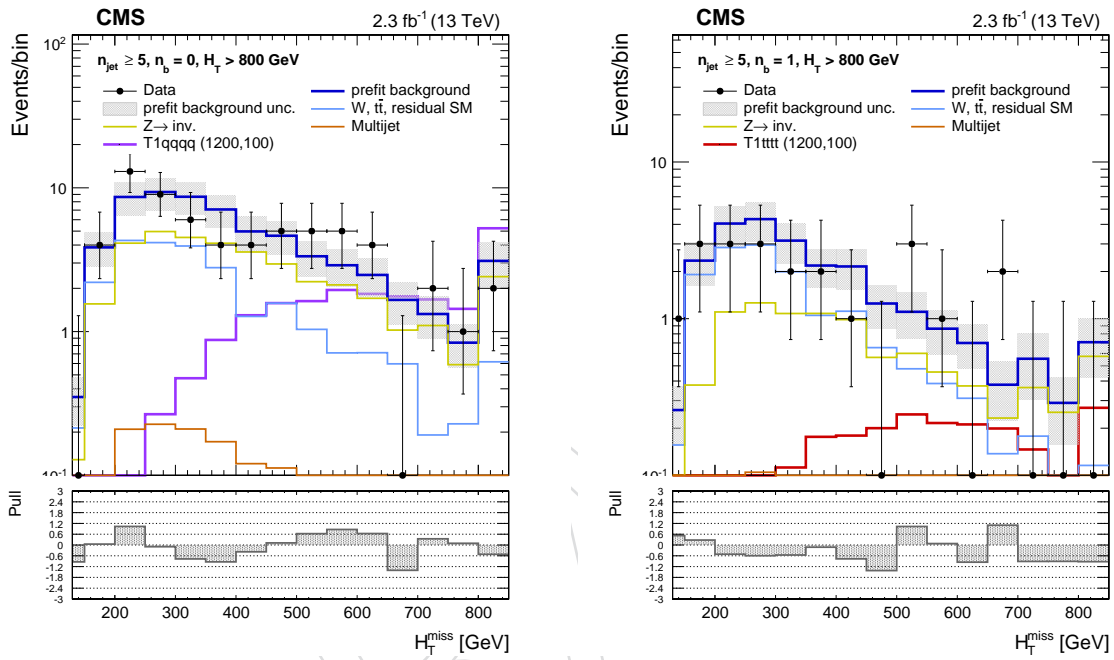


Figure 6: Event yields observed in data (solid circles) and “pre-fit” SM expectations with their associated uncertainties (blue histogram with shaded band) as a function of H_T^{miss} for events in the signal region that satisfy $n_{\text{jet}} \geq 5$, $H_T > 800$ GeV, and (Left) $n_b = 0$ or (Right) $n_b = 1$. For illustration only, the expectations for one of two benchmark models (T1qqqq with $m_{\tilde{g}} = 1200$ GeV and $m_{\tilde{\chi}_1^0} = 100$ GeV, T1tttt with $m_{\tilde{g}} = 1200$ GeV and $m_{\tilde{\chi}_1^0} = 100$ GeV) are superimposed on the SM-only expectations. The bottom panels indicate the significance of deviations observed in data with respect to both the “pre-fit” SM expectations, expressed in terms of the total uncertainty in the SM expectations.

8 Interpretations

8.1 Specification for simplified models

The results of the search are used to constrain simplified supersymmetric models [77–79]. Each model assumes the pair production of gluinos or squarks and their subsequent prompt decays to SM particles and the LSP ($\tilde{\chi}_1^0$) with a 100% branching ratio (unless indicated otherwise). The gluino decays contain intermediate on-shell sparticle states (such as the top squark, \tilde{t} , or the chargino, $\tilde{\chi}_1^\pm$) for a subset of the models. All other sparticles are assumed to be too heavy ($m_{\tilde{g}}/m_{\tilde{q}} = 10$ TeV) to be produced directly. Three-body decays of gluinos are assumed to occur via off-shell squarks of light or heavy flavour. Off-shell decays are processed by PYTHIA in a single three- or four-body step, without taking into account of the width or polarization of the parent: this is true for the top squark four-body decay ($\tilde{t} \rightarrow b\bar{f}\bar{f}'\tilde{\chi}_1^0$), as well as the three-body decay of the chargino ($\tilde{\chi}_1^\pm \rightarrow f\bar{f}'\tilde{\chi}_1^0$), where f and f' are fermions produced in the decay of an intermediate off-shell W boson.

Fourteen unique production and decay modes are considered, which yield a range of topologies and final states (with only the all-jet final state considered in this search). Each class of simplified model is identified by a label that indicates the topology and final state, and scans in the gluino or squark ($m_{\tilde{g}}/m_{\tilde{q}}$) and LSP ($m_{\tilde{\chi}_1^0}$) mass parameter space are performed. Table 4 summarises the production and decay modes, as well as any additional assumptions that define the simplified models. The models can be categorised according to the following descriptions: the gluino-mediated and direct production of light-flavour squarks; the gluino-mediated production of off-shell third-generation squarks; the “natural” gluino-mediated production of on-shell top squarks; and the direct production of on-shell third-generation squarks. In the case of direct pair production of light-flavour squarks, two different assumptions on the theory production cross section are made. For the “eightfold” scenario (T2qq_8fold), the scalar partners to left- and right-handed quarks of the u, d, s, and c flavours are assumed to be light and degenerate in mass, with other squark states decoupled to a high mass. For the “onefold” scenario (T2qq_1fold), only a single light squark is assumed to participate in the interaction and all other squarks are decoupled to a high mass.

Under the background + signal hypothesis, and in the presence of a non-zero signal contribution, a modified frequentist approach is used to determine upper limits at 95% confidence level (CL) on the cross section, σ_{UL} (pb), to produce pairs of supersymmetric particles as a function of the parent sparticle and the LSP masses. The potential contributions from a new-physics signal to each of the signal and control regions are considered, even though the only significant contribution occurs in the signal region and not the control region (i.e. signal contamination). The approach is based on the one-sided (LHC-style) profile likelihood ratio as the test statistic, the CL_s criterion [80, 81], and asymptotic formulae [82] are utilised to approximate the distributions of the test statistics under the SM background-only and signal + background hypotheses.

8.2 Acceptances and uncertainties

The experimental acceptance times efficiency ($\mathcal{A} \times \epsilon$) and its uncertainty are evaluated independently for each model class as a function of ($m_{\text{SUSY}}, m_{\text{LSP}}$). Table 5 summarises $\mathcal{A} \times \epsilon$ for a number of benchmark models, each chosen to be near the limit of search sensitivity. For each topology, typically two different pairs of parent sparticle and LSP masses ($m_{\text{SUSY}}, m_{\text{LSP}}$) are chosen that are characterised by a large and a smaller (i.e. “compressed”) difference in parent sparticle and LSP masses. The four most sensitive event categories, defined in terms of n_{jet} , are used to determine σ_{UL} . The categories used per benchmark model are listed in Table 5, along

Table 4: A summary of the simplified supersymmetric models used to interpret the results of this search. All on-shell sparticles in the decay are stated.

Model class	Production	Decay	Additional assumptions
<i>Glino-mediated and direct production of light-flavour squarks</i>			
T1qqqq	$pp \rightarrow \tilde{g}\tilde{g}$	$\tilde{g} \rightarrow \bar{q}q\tilde{\chi}_1^0$	–
T2qq_8fold	$pp \rightarrow \tilde{q}\tilde{q}$	$\tilde{q} \rightarrow q\tilde{\chi}_1^0$	$m_{\tilde{q}} = m_{\tilde{q}_L} = m_{\tilde{q}_R}, \tilde{q} = \{\tilde{u}, \tilde{d}, \tilde{s}, \tilde{c}\}$
T2qq_1fold	$pp \rightarrow \tilde{q}\tilde{q}$	$\tilde{q} \rightarrow q\tilde{\chi}_1^0$	$m_{\tilde{q}(\tilde{q} \neq \tilde{u}_L)} \gg m_{\tilde{u}_L}$
<i>Glino-mediated production of off-shell third-generation squarks</i>			
T1bbbb	$pp \rightarrow \tilde{g}\tilde{g}$	$\tilde{g} \rightarrow \bar{b}b\tilde{\chi}_1^0$	–
T1tttt	$pp \rightarrow \tilde{g}\tilde{g}$	$\tilde{g} \rightarrow \bar{t}t^* \rightarrow \bar{t}t\tilde{\chi}_1^0$	–
T1ttbb	$pp \rightarrow \tilde{g}\tilde{g}$	$\tilde{g} \rightarrow \bar{t}b\tilde{\chi}_1^\pm \rightarrow \bar{t}bW^*\tilde{\chi}_1^0$	$m_{\tilde{\chi}_1^\pm} - m_{\tilde{\chi}_1^0} = 5 \text{ GeV}$
<i>Natural gluino-mediated production of on-shell top squarks</i>			
T5tttt_DM175	$pp \rightarrow \tilde{g}\tilde{g}$	$\tilde{g} \rightarrow \bar{t}t \rightarrow \bar{t}t\tilde{\chi}_1^0$	$m_{\tilde{t}} - m_{\tilde{\chi}_1^0} = 175 \text{ GeV}$
T5ttcc	$pp \rightarrow \tilde{g}\tilde{g}$	$\tilde{g} \rightarrow \bar{t}t \rightarrow \bar{t}c\tilde{\chi}_1^0$	$m_{\tilde{t}} - m_{\tilde{\chi}_1^0} = 20 \text{ GeV}$
<i>Direct production of on-shell third-generation squarks</i>			
T2bb	$pp \rightarrow \tilde{b}\tilde{b}$	$\tilde{b} \rightarrow b\tilde{\chi}_1^0$	–
T2tb	$pp \rightarrow \tilde{t}\tilde{t}$	$\tilde{t} \rightarrow t\tilde{\chi}_1^0$ or $b\tilde{\chi}_1^\pm \rightarrow bW^*\tilde{\chi}_1^0$	$\mathcal{BR} = 50/50\%, m_{\tilde{\chi}_1^\pm} - m_{\tilde{\chi}_1^0} = 5 \text{ GeV}$
T2tt	$pp \rightarrow \tilde{t}\tilde{t}$	$\tilde{t} \rightarrow t\tilde{\chi}_1^0$	–
T2cc	$pp \rightarrow \tilde{t}\tilde{t}$	$\tilde{t} \rightarrow c\tilde{\chi}_1^0$	$10 < m_{\tilde{t}} - m_{\tilde{\chi}_1^0} < 80 \text{ GeV}$
T2tt_degen	$pp \rightarrow \tilde{t}\tilde{t}$	$\tilde{t} \rightarrow bW^*\tilde{\chi}_1^0$	$10 < m_{\tilde{t}} - m_{\tilde{\chi}_1^0} < 80 \text{ GeV}$
T2tt_mixed	$pp \rightarrow \tilde{t}\tilde{t}$	$\tilde{t} \rightarrow c\tilde{\chi}_1^0$ or $bW^*\tilde{\chi}_1^0$	$\mathcal{BR} = 50/50\%, 10 < m_{\tilde{t}} - m_{\tilde{\chi}_1^0} < 80 \text{ GeV}$

with $\mathcal{A} \times \varepsilon$ determined for these four categories.

Contributions from several sources to the uncertainty in $\mathcal{A} \times \varepsilon$ are considered. Each source of uncertainty is included in the likelihood function via alternative shapes to the nominal H_T^{miss} templates evaluated from simulated signal events categorised according to n_{jet} , n_b , and H_T . Correlations are taken into account where appropriate, including those relevant to signal contamination in the control regions. The morphing scheme that interpolates between the nominal and alternative H_T^{miss} templates, described in Section 7, is also used for the simulated signal samples.

In addition to the uncertainty in the integrated luminosity of 2.7%, the following sources of uncertainty are dominant: the statistical uncertainty arising from the finite size of simulated signal samples, the modelling of initial-state radiation (ISR), the corrections to jet energies (JEC) evaluated in simulation, and the modelling of scale factors ($\text{SF}_{b\text{-tag}}$) applied to simulated event samples that correct for differences in the efficiency and misidentification probability of b quark jets. The magnitude of each contribution depends on the model and the masses of the parent sparticle and LSP.

The $\mathcal{A} \times \varepsilon$ for models with small mass splittings (e.g. $m_{\tilde{q}} - m_{\tilde{\chi}_1^0} \lesssim m_t$) is due in large part to ISR, the modelling of which is evaluated by comparing the simulated and measured p_T spectra of the system recoiling against the ISR jets in $t\bar{t}$ events, using the technique described in Ref. [83]. The uncertainty can be as large as $\sim 30\%$, and is the dominant systematic uncertainty for systems with a compressed mass spectrum. Uncertainties in the jet energy scale, as large as $\sim 40\%$, can also be dominant for models characterised by high jet multiplicities in the final state. The uncertainties in $\text{SF}_{b\text{-tag}}$ can be as large as $\sim 25\%$. Table 5 summarises these dominant contributions to the uncertainty in $\mathcal{A} \times \varepsilon$ for a range of benchmark models. Characteristic

Table 5: A summary of benchmark simplified models, the most sensitive n_{jet} categories, and representative values for the corresponding experimental acceptance times efficiency ($\mathcal{A} \times \varepsilon$), the dominant systematic uncertainties, the theory production cross section (σ_{theory}), and the expected and observed upper limits on the production cross section, expressed in terms of the signal strength parameter (μ).

Benchmark models		Most sensitive	$\mathcal{A} \times \varepsilon$	Systematic uncertainties [%]				σ_{theory}	μ (95% CL)	
$(m_{\text{SUSY}}, m_{\text{LSP}})$ [GeV]		n_{jet} categories	[%]	MC stat.	ISR	JEC	SF _{b-tag}	[fb]	Exp.	Obs.
T1qqqq	(1300, 100)	$\geq 5, 4, 3, 2$	9.4	7-30	~ 2	4-21	2-14	46.1	0.79	0.76
	(900, 700)	$\geq 5, \geq 5a, 4, 4a$	5.6	10-33	1-13	1-26	1-10	677	0.58	0.44
T2qq-8fold	(1050, 100)	$\geq 5, 3, 4, 2$	17.9	7-33	1-4	3-16	1-11	35.2	0.90	0.63
	(650, 550)	$\geq 5, 4, \geq 5a, 4a$	2.6	10-28	1-16	2-29	1-6	864	0.93	0.80
T2qq-1fold	(600, 50)	$\geq 5, 3, 2, 4$	13.4	5-33	1-5	1-30	1-8	177	0.78	0.84
	(400, 250)	$\geq 5, 4, \geq 5a, 3$	2.9	8-30	1-8	3-25	1-7	1849	0.73	0.71
T1bbbb	(1500, 100)	$\geq 5, 4, 3, 2$	10.1	5-17	1-2	1-12	2-22	14.2	0.81	0.79
	(1000, 800)	$\geq 5, 4, \geq 5a, 4a$	4.9	8-31	1-17	1-40	1-14	325	0.33	0.32
T1tttt	(1300, 100)	$\geq 5, \geq 5a, 4, 3$	2.4	7-16	1-2	2-7	2-12	46.1	1.00	1.89
	(800, 400)	$\geq 5, \geq 5a, 4, 4a$	0.6	7-27	1-2	3-45	1-8	1490	0.56	1.03
T1ttbb	(1300, 100)	$\geq 5, 4, 3, \geq 5a$	3.8	9-32	1-2	3-16	2-19	46.1	0.60	0.91
	(1000, 700)	$\geq 5, \geq 5a, 4, 3$	3.4	9-30	1-9	3-65	1-14	325	0.51	0.70
T5tttt-DM175	(800, 100)	$\geq 5, \geq 5a, 3, 4$	0.2	12-20	2-4	3-5	1-6	1490	0.69	1.19
	(700, 400)	$\geq 5, \geq 5a, 4, 4a$	0.2	20-29	2-10	8-10	1-2	3530	1.00	1.35
T5ttcc	(1200, 200)	$\geq 5, 4, 3, \geq 5a$	4.9	6-25	5-25	3-21	1-24	85.6	0.58	0.87
	(750, 600)	$\geq 5, \geq 5a, 4, 4a$	1.0	9-23	1-4	5-21	1-3	2270	0.89	0.72
T2bb	(800, 50)	$2, 3, 4, \geq 5$	1.5	5-31	2-6	1-21	1-23	28.3	0.96	1.06
	(375, 300)	$\geq 5, 4, 3a, 3$	0.1	8-33	1-10	3-25	1-7	2610	0.67	0.87
T2tb	(600, 50)	$\geq 5, 4, 3, 2$	6.1	3-28	1-3	1-22	1-17	175	0.70	1.35
	(350, 225)	$\geq 5, 4, 3, 3a$	1.0	9-33	1-4	2-41	1-8	3790	0.79	0.88
T2tt	(700, 50)	$\geq 5, 4, 3, \geq 5a$	8.1	8-33	1-4	2-22	1-21	67.0	0.90	1.19
	(350, 100)	$\geq 5, \geq 5a, 4a, 4$	1.4	7-31	1-1	1-28	1-7	3790	0.44	0.50
T2cc	(325, 305)	$\geq 5, 4, 3, 2$	0.8	3-32	1-27	1-27	1-12	5600	0.92	0.68
T2-degen	(300, 290)	$3, 4, \geq 5, 2$	0.9	2-27	1-27	1-25	1-12	8520	0.56	0.41
T2tt-mixed	(300, 250)	$\geq 5, 4, \geq 5a, 4a$	0.4	3-33	1-27	1-33	1-13	8520	0.99	0.58

values for each model are expressed in terms of a range that is representative of the values across all bins of the signal region. The upper bound for each range may be subject to moderate statistical fluctuations.

Further uncertainties with subdominant contributions are considered on a similar footing. The uncertainties in the efficiency of identifying well-reconstructed, isolated leptons are considered, with a typical magnitude of $\sim 5\%$ and treated as anti-correlated between the signal and control regions. The uncertainty of 5% in σ_{MB} is propagated through to the reweighting procedure to account for differences between the simulated and data-derived measurements of the pileup distributions. Finally, uncertainties in the simulation modelling of the efficiencies of the trigger strategy employed by the search are typically $< 10\%$.

The choice of PDF set, or variations therein, predominantly affects $\mathcal{A} \times \varepsilon$ through changes in the p_T spectrum of the system recoil, which is covered by the ISR uncertainty, hence no additional uncertainty is adopted. Uncertainties in $\mathcal{A} \times \varepsilon$ due to variations in the renormalisation and factorisation scales are determined to be relatively small. In both cases, contributions to the

uncertainty in the theory production cross section are considered.

8.3 Cross section and mass exclusions

The upper limits on the signal production cross section are evaluated at a 95% CL for each of the aforementioned benchmark models. The limits are expressed in terms of the signal strength parameter, μ , which is determined relative to the theory cross section that is calculated at NLO+NLL accuracy. The limits are summarised in Table 5. Expected limits on μ are also listed, which are determined using an asimov data set. All benchmark models are disfavoured based on expectations. The observed limits fluctuate around the expected μ values, with some models exhibiting a moderately weaker-than-expected limit.

Figures 7 and 8 summarise the disfavoured regions of the mass parameter space for the fourteen classes of simplified model. These regions are derived by comparing the upper limits on the measured fiducial cross section, corrected for the experimental $\mathcal{A} \times \varepsilon$, with the theory cross sections calculated at NLO+NLL accuracy in α_s . The former cross section value is determined as a function of $m_{\tilde{g}}$ or $m_{\tilde{q}}$ and $m_{\tilde{\chi}_1^0}$, while the latter has a dependence solely on $m_{\tilde{g}}$ or $m_{\tilde{q}}$. The exclusion of models is evaluated using observed data counts in the signal region (solid contours) and also expected counts based on an asimov data set (dashed contours).

Figure 7 (top) shows the excluded mass parameter space for models that assume the gluino-mediated or direct production of light-flavour squarks. The excluded region extends to higher masses for the gluino-mediated production of light-flavour squarks (T1qqqq), with respect to the direct pair production when assuming an eightfold degeneracy in mass (T2qq.8fold), due to a combination of a higher gluino pair production cross section and a final state characterised by higher jet multiplicities, which are exploited to provide better signal-to-background separation. The excluded mass region is significantly reduced when assuming only a single light squark (T2qq.1fold), with limits weakening due to the lower production cross section, compounded by the reduced signal-to-background ratios achieved in the core of distributions in the discriminating variables.

Figure 7 (bottom) shows the exclusion contours for models that assume the gluino-mediated pair production of off-shell third-generation squarks. For the topologies T1ttttt and T1bbbb, each gluino is assumed to undergo a three-body decay via, respectively, an off-shell top or bottom squark to a quark-antiquark pair of the same flavour and the $\tilde{\chi}_1^0$. In the case of T1ttbb, each gluino is assumed to undergo a three-body decay to an on-shell chargino, $\tilde{\chi}_1^\pm$, a bottom quark, and an antitop quark. The chargino mass is defined relative to the neutralino mass via the expression $m_{\tilde{\chi}_1^\pm} - m_{\tilde{\chi}_1^0} = 5 \text{ GeV}$. The chargino decays promptly to the $\tilde{\chi}_1^0$ and an off-shell W boson. The excluded mass regions differ significantly for these topologies, primarily due to the different number of (on-shell) W bosons in their final states, resulting in the highest $\mathcal{A} \times \varepsilon$ for T1bbbb and lowest for T1ttttt. Further, $\mathcal{A} \times \varepsilon$ has a strong dependence on jet multiplicity, which is highest for T1ttttt, due to the $\Delta\phi_{\min}^*$ variable. An additional feature for T1ttbb is the weakening of the mass limit at low values of $m_{\tilde{\chi}_1^0}$, when $m_{\tilde{\chi}_1^\pm} = m_{\tilde{\chi}_1^0} + 5 \text{ GeV} \lesssim m_t$. In this scenario, the $\tilde{\chi}_1^\pm$ (and hence $\tilde{\chi}_1^0$) is not highly Lorentz boosted relative to the top quark resulting from the three-body decay of the gluino. Hence, two $\tilde{\chi}_1^0$ sparticles do not carry away significant \vec{p}_T^{miss} , which is instead realised through W boson decays to neutrinos and “lost” leptons or τ leptons that decay to neutrinos and hadrons. The observed mass limits for these topologies are up to ~ 2 standard deviations weaker than the expected limits. These differences are due to upward fluctuations in data for two contiguous bins that satisfy the requirements $n_{\text{jet}} \geq 5$, $n_b \geq 2$, and $H_T > 800 \text{ GeV}$. This region has the highest sensitivity to models involving gluino production and decays to third-generation quarks (via on- or off-shell

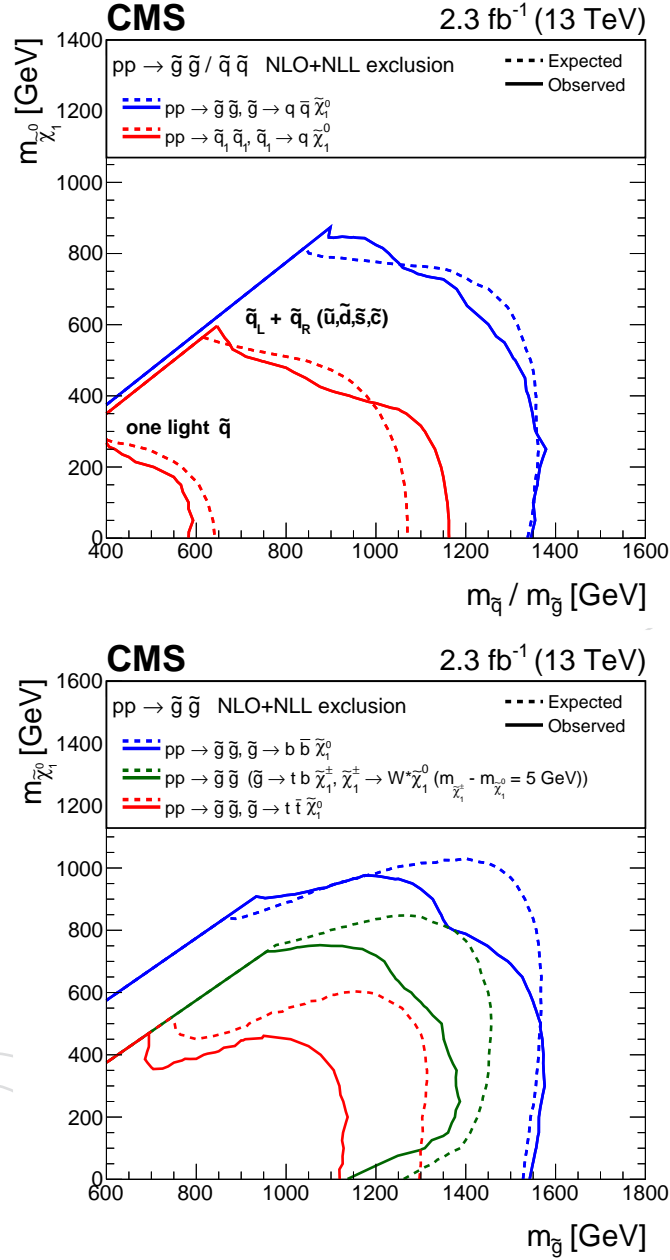


Figure 7: Observed and expected mass exclusions at 95% CL (indicated, respectively, by solid and dashed contours) for various classes of simplified models. (Top) The pair production of gluino-mediated or direct pair production of light-flavour squarks. The two scenarios involve, respectively, the decay $\tilde{g} \rightarrow \bar{q}q\tilde{\chi}_1^0$ (T1qqqq) and $\tilde{q} \rightarrow q\tilde{\chi}_1^0$, and the latter involves two assumptions on the mass degeneracy of the squarks (T2qq_8fold and T2qq_1fold). (Bottom) Three scenarios involving the gluino-mediated pair production of off-shell third-generation squarks: $\tilde{g} \rightarrow b\bar{b}\tilde{\chi}_1^0$ (T1bbbb), $\tilde{g} \rightarrow t\bar{t}\tilde{\chi}_1^0 \rightarrow t\bar{t}W^*\tilde{\chi}_1^0$ (T1tttt), and $\tilde{g} \rightarrow t\bar{b}\tilde{\chi}_1^\pm \rightarrow t\bar{b}W^*\tilde{\chi}_1^0$ (T1tbb).

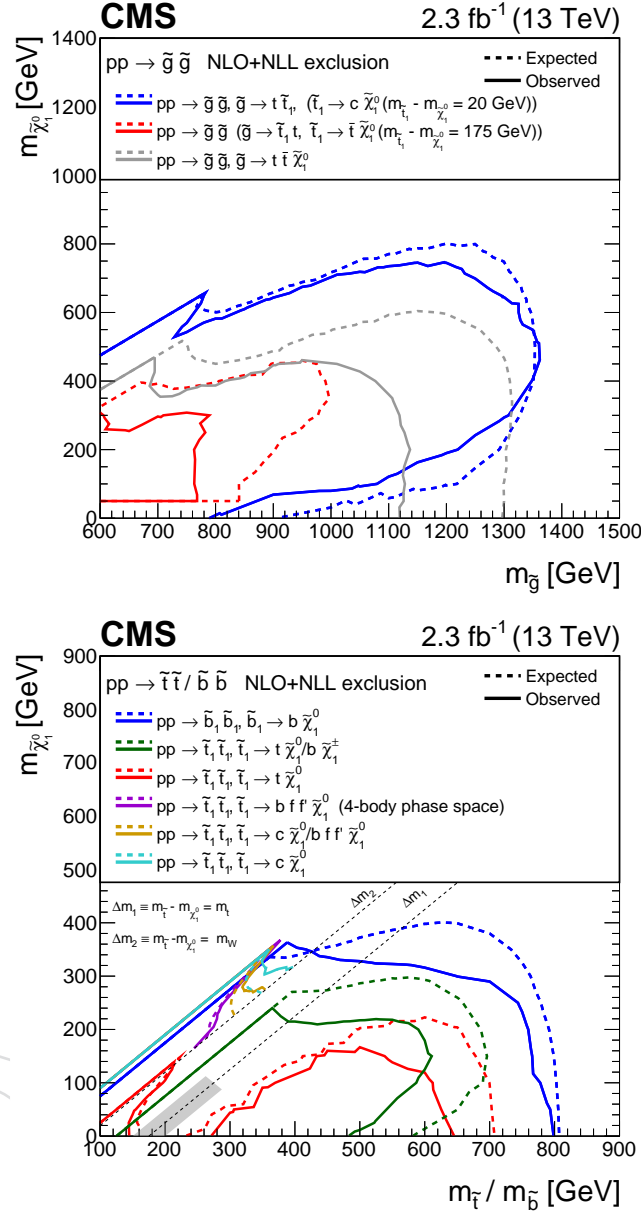


Figure 8: Observed and expected mass exclusions at 95% CL (indicated, respectively, by solid and dashed contours) for a number of simplified models. (Top) Two scenarios involving the gluino-mediated pair production of on-shell top squarks: $\tilde{g} \rightarrow \tilde{t}\tilde{t} \rightarrow \tilde{t}\tilde{t}\tilde{\chi}_1^0$ with $m_{\tilde{t}} - m_{\tilde{\chi}_1^0} = 175 \text{ GeV}$ (T5ttttt_DM175) and $\tilde{g} \rightarrow \tilde{t}\tilde{t} \rightarrow \tilde{t}c\tilde{\chi}_1^0$ with $m_{\tilde{t}} - m_{\tilde{\chi}_1^0} = 20 \text{ GeV}$ (T5ttcc). Also shown, for comparison, is T1ttttt. (Bottom) Six scenarios involving the direct pair production of third-generation squarks. The first scenario involves the pair production of bottom squarks, $\tilde{b} \rightarrow b\tilde{\chi}_1^0$ (T2bb). Two scenarios involve the decay of top squark pairs as follows: $\tilde{t} \rightarrow t\tilde{\chi}_1^0$ or $\tilde{t} \rightarrow b\tilde{\chi}_1^\pm \rightarrow bW^*\tilde{\chi}_1^0$ with $m_{\tilde{\chi}_1^\pm} - m_{\tilde{\chi}_1^0} = 5 \text{ GeV}$ and $\mathcal{BR} = 50/50\%$ (T2tb), or $\tilde{t} \rightarrow t\tilde{\chi}_1^0$ (T2tt). The final three scenarios consider top squark decays under the assumption $10 < m_{\tilde{t}} - m_{\tilde{\chi}_1^0} < 80 \text{ GeV}$: $\tilde{t} \rightarrow c\tilde{\chi}_1^0$ (T2cc), $\tilde{t} \rightarrow bW^*\tilde{\chi}_1^0$ (T2tt_degen), and $\tilde{t} \rightarrow c\tilde{\chi}_1^0$ or $\tilde{t} \rightarrow bW^*\tilde{\chi}_1^0$ with $\mathcal{BR} = 50/50\%$ (T2tt_mixed). The grey shaded region denotes T2tt models that are not considered for interpretation.

squarks). The observed counts are consistent with statistical fluctuations and the events do not exhibit anomalous nonphysical behaviours. The events are distributed in H_T^{miss} consistent with expectation, hence models characterised by high values of H_T^{miss} , such as T1bbbb with $m_{\tilde{g}} \gg m_{\tilde{\chi}_1^0}$ or $m_{\tilde{g}} \approx m_{\tilde{\chi}_1^0}$, are less compatible with the data counts in this high- n_{jet} , n_b , and H_T region.

Figure 8 (top) shows exclusion contours for models that assume gluino pair production, with each gluino decaying to a top quark and an on-shell top squark, the latter of which decays to SM particles and the LSP, $\tilde{\chi}_1^0$. As discussed earlier, these models can be considered as representations of a “natural” solution to the little hierarchy problem. Two different scenarios are considered for the decay of the top squarks. The T5ttttt_DM175 models assume a two-body decay to a top quark and the $\tilde{\chi}_1^0$, with the top squark mass defined relative to the $\tilde{\chi}_1^0$ as $m_{\tilde{t}} - m_{\tilde{\chi}_1^0} = m_t$. Models that satisfy $m_{\tilde{\chi}_1^0} < 50 \text{ GeV}$ are not considered here, as the $\tilde{\chi}_1^0$ particles carry very little momentum. The T5ttcc models assume $m_{\tilde{t}} - m_{\tilde{\chi}_1^0} = 20 \text{ GeV}$ and two-body decays to a charm quark and the $\tilde{\chi}_1^0$.

Finally, Fig. 8 (bottom) shows exclusion contours for models that assume the direct production of pairs of third-generation squarks. For the T2bb models, bottom squarks are pair produced and each decays to a bottom quark and the $\tilde{\chi}_1^0$. The T2tt models assume top squarks are pair produced and each is assumed to undergo a two- or three-body decay to, respectively, a top quark and the $\tilde{\chi}_1^0$ when $m_{\tilde{t}} - m_{\tilde{\chi}_1^0} > m_t$ is satisfied, or a b quark, an on-shell W boson, and the $\tilde{\chi}_1^0$ for the condition $m_W < m_{\tilde{t}} - m_{\tilde{\chi}_1^0} < m_t$. Models that satisfy $|m_{\tilde{t}} - m_t - m_{\tilde{\chi}_1^0}| < 25 \text{ GeV}$ and $m_{\tilde{t}} + m_{\tilde{\chi}_1^0} < 375 \text{ GeV}$ are not considered here, as σ_{UL} is a strong function of $m_{\tilde{t}} - m_{\tilde{\chi}_1^0}$ in this low- $m_{\tilde{t}}$ region, due to the high levels of signal contamination found in the $\mu + \text{jets}$ control region for models that resemble the $t\bar{t}$ background in terms of their topological and kinematic properties. The T2tb models also assume the pair production of top squarks, with each undergoing a two-body decay to either a top quark and the $\tilde{\chi}_1^0$, or a bottom quark and the $\tilde{\chi}_1^\pm$, with equal branching ratios $\mathcal{BR}(\tilde{t} \rightarrow t\tilde{\chi}_1^0) = \mathcal{BR}(\tilde{t} \rightarrow b\tilde{\chi}_1^\pm) = 50\%$. As for the T1ttbb models, the chargino mass is defined relative to the neutralino mass via the expression $m_{\tilde{\chi}_1^\pm} - m_{\tilde{\chi}_1^0} = 5 \text{ GeV}$, and the chargino decays promptly to the $\tilde{\chi}_1^0$ and an off-shell W boson. The excluded mass regions differ significantly for the T2bb, T2tb, and T2tt topologies, in an analogous way to the T1bbbb, T1ttbb, and T1tttt models described above. The difference in the mass exclusions is due primarily to the different number of (on-shell) W bosons in the final states, which affects $\mathcal{A} \times \varepsilon$ through the presence of leptons from the decay of the W boson. An additional feature for T2tb is the weakening of the mass limit at low values of $m_{\tilde{\chi}_1^0}$, when $m_{\tilde{\chi}_1^\pm} = m_{\tilde{\chi}_1^0} + 5 \text{ GeV} \lesssim m_t$. Moderately weaker-than-expected mass limits are observed for all models involving two-body decays, which is traced to mild upward fluctuations in data for events satisfying $n_{\text{jet}} = 2$, $n_b = 2$, and $350 < H_T < 500 \text{ GeV}$.

Figure 8 (bottom) also shows exclusion contours for models that assume the pair production of top squarks but a near-mass-degenerate system that satisfies $10 \text{ GeV} < m_{\tilde{t}} - m_{\tilde{\chi}_1^0} < m_W$. Two decays of the top squark are considered. The T2cc and T2tt_degen models assume two- and four-body decays of the top squark to, respectively, a charm quark and the $\tilde{\chi}_1^0$, or to via an off-shell W boson. A third class of models, T2tt_mixed, assumes both these decay modes with an equal branching ratio, $\mathcal{BR}(\tilde{t} \rightarrow c\tilde{\chi}_1^0) = \mathcal{BR}(\tilde{t} \rightarrow b\tilde{\chi}_1^0) = 50\%$. For T2cc, the excluded mass region is relatively stable as a function of the mass splitting $\Delta m = m_{\tilde{t}} - m_{\tilde{\chi}_1^0}$, with \tilde{t} masses excluded up to 400 GeV. For T2tt_degen, the excluded mass region is strongly dependent on Δm , weakening considerably for increasing values of Δm due to the increased momentum phase space available to leptons produced in the four-body decay. The T2tt_mixed models

Table 6: Summary of the mass limits obtained for the fourteen classes of simplified models. The limits indicate the strongest observed and expected (in parentheses) mass exclusions in \tilde{g} , \tilde{q} , \tilde{b} , \tilde{t} , and $\tilde{\chi}_1^0$. The quoted values have uncertainties of ± 25 GeV and ± 10 GeV for models involving the pair production of, respectively, gluinos and squarks.

Model class	Parent sparticle	Best mass limit [GeV]	
		$\tilde{g}/\tilde{q}/\tilde{b}/\tilde{t}$	$\tilde{\chi}_1^0$
T1qqqq	\tilde{g}	1375 (1350)	875 (850)
T2qq-8fold	\tilde{q}	1150 (1075)	600 (550)
T2qq-1fold	\tilde{q}	575 (650)	275 (275)
T1bbbb	\tilde{g}	1575 (1575)	975 (1025)
T1tttt	\tilde{g}	1125 (1325)	475 (600)
T1ttbb	\tilde{g}	1375 (1450)	750 (850)
T5tttt_DM175	\tilde{g}	800 (1000)	300 (450)
T5ttcc	\tilde{g}	1350 (1350)	700 (800)
T2bb	\tilde{b}	800 (800)	360 (400)
T2tb	\tilde{t}	610 (690)	240 (300)
T2tt (3-body)	\tilde{t}	670 (720)	210 (240)
T2tt (2-body)	\tilde{t}	280 (280)	200 (200)
T2cc	\tilde{t}	400 (350)	310 (340)
T2tt_degen	\tilde{t}	370 (360)	360 (350)
T2tt_mixed	\tilde{t}	360 (350)	350 (340)

exhibit an intermediate behaviour. Mass limits for all three model classes converge for the smallest mass splitting considered, $\Delta m = 10$ GeV, when the SM particles from the \tilde{t} decay are extremely soft and outside the experimental acceptance. An approximately contiguous mass exclusion limit is observed across the transition from the T2tt_degen four-body to the T2tt three-body decay of the \tilde{t} , as the top quark moves on-shell. The excluded mass region weakens further as $\Delta m \rightarrow m_t$.

Table 6 summarises the strongest expected and observed excluded $m_{\tilde{g}}$ or $m_{\tilde{q}}$ and $m_{\tilde{\chi}_1^0}$ masses for each class of simplified model.

9 Summary

An inclusive search for new-physics phenomena is reported, based on data from pp collisions at $\sqrt{s} = 13$ TeV. The data are recorded with the CMS detector and correspond to an integrated luminosity of $2.3 \pm 0.1 \text{ fb}^{-1}$. The final states analysed contain one or more jets with large transverse momenta (p_T) and a significant imbalance in transverse momentum, as expected from the production of massive coloured sparticles, each decaying to SM particles and the lightest stable, weakly-interacting supersymmetric particle.

Signal candidate events are categorised according to the number of reconstructed jets, and the number of jets identified as originating from b quarks, and the scalar (H_T) and vector (H_T^{miss}) sums of the transverse momenta of jets. The search employs the use of several kinematic variables, including α_T and $\Delta\phi_{\text{min}}^*$, to suppress the background from QCD multijet production to the percent level with respect to other non-multijet SM backgrounds, which are dominated by vector boson and top-antitop production. The α_T variable is also employed in the trigger logic that is used to record the candidate signal events, which allows the use of low thresholds for the momentum sums, $H_T > 200$ GeV and $H_T^{\text{miss}} \gtrsim 130$ GeV. These low thresholds, in addition to the inclusion of final states containing a single jet, maximise the experimental acceptance

to new-physics processes, such as low-mass squark signatures, nearly mass-degenerate SUSY models, and other new-physics phenomena, such as DM models that postulate the direct production of stable, weakly interacting, massive particles in pp collisions.

The sums of the standard model backgrounds are estimated from a simultaneous binned likelihood fit to the observed yields for samples of events categorised according to n_{jet} , n_b , H_T , and H_T^{miss} in the signal region and in $\mu + \text{jets}$, $\mu\mu + \text{jets}$, and $\gamma + \text{jets}$ control regions. The observed yields in the signal are found to be in agreement with the expected contributions from standard model processes. The search result is interpreted in the mass parameter space of fourteen simplified supersymmetric models that assume the pair production of gluinos or squarks and a range of decay modes. The models cover scenarios that involve the gluino-mediated or direct production or light- or heavy-flavour squarks, spectra with intermediate sparticle states and branching ratios, “natural” spectra with gluinos and on-shell top squarks, and nearly mass-degenerate spectra.

The increase in the centre-of-mass energy of the LHC, from $\sqrt{s} = 8$ to 13 TeV, provides a significant gain in sensitivity to heavy particle states such as gluinos. In the case of pair production of gluinos that each decays, via an off-shell b squark, to the b quark and the LSP, models with masses up to ~ 1.6 TeV and ~ 1.0 TeV are excluded for, respectively, the gluino and LSP, which is an improvement of, respectively, ~ 250 and ~ 300 GeV with respect to Run 1. In the case of direct pair production, models with masses up to ~ 800 GeV and ~ 350 GeV are excluded for, respectively, the b squark and LSP. These mass limits are sensitive to the assumptions on the squark flavour and the presence of intermediate states, such as charginos.

Finally, a comprehensive study of nearly mass-degenerate models involving top squark pair production is performed. The two decay modes open to the top squark are considered: the loop-induced two-body decay to the neutralino and one c quark, and the four-body decay to the neutralino, one b quark, and an off-shell W boson. A third scenario is considered, when the two modes are simultaneously open each with a branching ratio of 50%. Masses of the top squark and LSP up to, respectively, 400 GeV and 360 GeV are excluded, depending on the decay modes considered.

In summary, the analysis provides sensitivity across a large region of the “natural” supersymmetric parameter space, as characterised by interpretations with several simplified models. In particular, these studies improve on existing limits for nearly mass-degenerate models involving the production of pairs of top squarks.

References

- [1] Y. A. Gol’fand and E. P. Likhtman, “Extension of the Algebra of Poincaré Group Generators and Violation of p Invariance”, *JETP Lett.* **13** (1971) 323.
- [2] J. Wess and B. Zumino, “Supergauge transformations in four dimensions”, *Nucl. Phys. B* **70** (1974) 39, doi:10.1016/0550-3213(74)90355-1.
- [3] R. Barbieri, S. Ferrara, and C. A. Savoy, “Gauge Models with Spontaneously Broken Local Supersymmetry”, *Phys. Lett. B* **119** (1982) 343, doi:10.1016/0370-2693(82)90685-2.
- [4] H. P. Nilles, “Supersymmetry, Supergravity and Particle Physics”, *Phys. Reports* **110** (1984) 1, doi:10.1016/0370-1573(84)90008-5.

- [5] S. Dimopoulos, S. Raby, and F. Wilczek, “Supersymmetry and the Scale of Unification”, *Phys. Rev. D* **24** (1981) 1681–1683, doi:10.1103/PhysRevD.24.1681.
- [6] L. E. Ibanez and G. G. Ross, “Low-Energy Predictions in Supersymmetric Grand Unified Theories”, *Phys. Lett. B* **105** (1981) 439–442, doi:10.1016/0370-2693(81)91200-4.
- [7] W. J. Marciano and G. Senjanovic, “Predictions of Supersymmetric Grand Unified Theories”, *Phys. Rev. D* **25** (1982) 3092, doi:10.1103/PhysRevD.25.3092.
- [8] S. Dawson, E. Eichten, and C. Quigg, “Search for Supersymmetric Particles in Hadron - Hadron Collisions”, *Phys. Rev. D* **31** (1985) 1581, doi:10.1103/PhysRevD.31.1581.
- [9] H. Haber and G. Kane, “The Search for Supersymmetry: Probing Physics Beyond the Standard Model”, *Phys. Reports* **117** (1987) 75, doi:10.1016/0370-1573(85)90051-1.
- [10] ATLAS Collaboration, “Observation of a new particle in the search for the Standard Model Higgs boson with the ATLAS detector at the LHC”, *Phys. Lett. B* **716** (2012) 1, doi:10.1016/j.physletb.2012.08.020, arXiv:1207.7214.
- [11] CMS Collaboration, “Observation of a new boson with mass near 125 GeV in pp collisions at $\sqrt{s} = 7$ and 8 TeV”, *JHEP* **06** (2013) 081, doi:10.1007/JHEP06(2013)081, arXiv:1303.4571.
- [12] E. Witten, “Dynamical Breaking of Supersymmetry”, *Nucl. Phys. B* **188** (1981) 513, doi:10.1016/0550-3213(81)90006-7.
- [13] S. Dimopoulos and H. Georgi, “Softly Broken Supersymmetry and SU(5)”, *Nucl. Phys. B* **193** (1981) 150, doi:10.1016/0550-3213(81)90522-8.
- [14] R. Barbieri and D. Pappadopulo, “S-particles at their naturalness limits”, *JHEP* **10** (2009) 061, doi:10.1088/1126-6708/2009/10/061, arXiv:0906.4546.
- [15] G. R. Farrar and P. Fayet, “Phenomenology of the Production, Decay, and Detection of New Hadronic States Associated with Supersymmetry”, *Phys. Lett. B* **76** (1978) 575, doi:10.1016/0370-2693(78)90858-4.
- [16] G. Jungman, M. Kamionkowski, and K. Griest, “Supersymmetric dark matter”, *Phys. Rept.* **267** (1996) 195–373, doi:10.1016/0370-1573(95)00058-5, arXiv:hep-ph/9506380.
- [17] K. Olive and the Particle Data Group, “Review of Particle Physics: Dark Matter”, *Chinese Physics C* **38** (2014) 090001.
- [18] A. Delgado et al., “The light stop window”, *Eur. Phys. J. C* **73** (2013) 2370, doi:10.1140/epjc/s10052-013-2370-5, arXiv:1212.6847.
- [19] C. Boehm, A. Djouadi, and Y. Mambrini, “Decays of the lightest top squark”, *Phys. Rev. D* **61** (2000) 095006, doi:10.1103/PhysRevD.61.095006, arXiv:hep-ph/9907428.
- [20] M. Carena, A. Freitas, and C. Wagner, “Light Stop Searches at the LHC in Events with One Hard Photon or Jet and Missing Energy”, *JHEP* **10** (2008) 109, doi:10.1088/1126-6708/2008/10/109, arXiv:0808.2298.

- [21] R. Grober, M. M. Muhlleitner, E. Popena, and A. Wlotzka, “Light Stop Decays: Implications for LHC Searches”, *Eur. Phys. J. C* **75** (2015) 420, doi:10.1140/epjc/s10052-015-3626-z, arXiv:1408.4662.
- [22] R. Grober, M. Muhlleitner, E. Popena, and A. Wlotzka, “Light stop decays into $Wb\tilde{\chi}_1^0$ near the kinematic threshold”, *Phys. Lett. B* **747** (2015) 144, doi:10.1016/j.physletb.2015.05.060, arXiv:1502.05935.
- [23] C. Boehm, A. Djouadi, and M. Drees, “Light scalar top quarks and supersymmetric dark matter”, *Phys. Rev. D* **62** (2000) 035012, doi:10.1103/PhysRevD.62.035012, arXiv:hep-ph/9911496.
- [24] C. Balazs, M. S. Carena, and C. Wagner, “Dark matter, light stops and electroweak baryogenesis”, *Phys. Rev. D* **70** (2004) 015007, doi:10.1103/PhysRevD.70.015007, arXiv:hep-ph/0403224.
- [25] S. P. Martin, “Compressed supersymmetry and natural neutralino dark matter from top squark-mediated annihilation to top quarks”, *Phys. Rev. D* **75** (2007) 115005, doi:10.1103/PhysRevD.75.115005, arXiv:hep-ph/0703097.
- [26] S. P. Martin, “Top squark-mediated annihilation scenario and direct detection of dark matter in compressed supersymmetry”, *Phys. Rev. D* **76** (2007) 095005, doi:10.1103/PhysRevD.76.095005, arXiv:0707.2812.
- [27] CMS Collaboration, “Search for Supersymmetry in pp Collisions at 7 TeV in Events with Jets and Missing Transverse Energy”, *Phys. Lett. B* **698** (2011) 196, doi:10.1016/j.physletb.2011.03.021, arXiv:1101.1628.
- [28] CMS Collaboration, “Search for Supersymmetry at the LHC in Events with Jets and Missing Transverse Energy”, *Phys. Rev. Lett.* **107** (2011) 221804, doi:10.1103/PhysRevLett.107.221804.
- [29] CMS Collaboration, “Search for supersymmetry in final states with missing transverse energy and 0, 1, 2, or ≥ 3 b-quark jets in 7 TeV pp collisions using the α_T variable”, *JHEP* **01** (2013) 077, doi:10.1007/JHEP01(2013)077.
- [30] CMS Collaboration, “Search for supersymmetry in hadronic final states with missing transverse energy using the variables α_T and b-quark multiplicity in pp collisions at $\sqrt{s} = 8$ TeV”, *EPJC* **01** (2013) 077, doi:10.1007/JHEP01(2013)077.
- [31] CMS Collaboration, “Search for top squark pair production in compressed-mass-spectrum scenarios in proton-proton collisions at $\sqrt{s} = 8$ TeV using the α_T variable”, (2016). arXiv:1605.0000. Submitted to *Phys. Lett. B*.
- [32] A. D. Martin, W. J. Stirling, R. S. Thorne, and G. Watt, “Heavy-quark mass dependence in global PDF analyses and 3- and 4-flavour parton distributions”, *Eur. Phys. J. C* **70** (2010) 51–72, doi:10.1140/epjc/s10052-010-1462-8, arXiv:1007.2624.
- [33] ATLAS Collaboration, “Summary of the searches for squarks and gluinos using $\sqrt{s} = 8$ TeV pp collisions with the ATLAS experiment at the LHC”, *JHEP* **10** (2015) 054, doi:10.1007/JHEP10(2015)054, arXiv:1507.05525.
- [34] CMS Collaboration, “Searches for supersymmetry based on events with b jets and four W bosons in pp collisions at 8 TeV”, *Phys. Lett. B* **745** (2015) 5–28, doi:10.1016/j.physletb.2015.04.002, arXiv:1412.4109.

- [35] CMS Collaboration, “Searches for Supersymmetry using the M_{T2} Variable in Hadronic Events Produced in pp Collisions at 8 TeV”, *JHEP* **05** (2015) 078, doi:10.1007/JHEP05(2015)078, arXiv:1502.04358.
- [36] ATLAS Collaboration, “Search for new phenomena in final states with large jet multiplicities and missing transverse momentum with ATLAS using $\sqrt{s} = 13$ TeV proton–proton collisions”, (2016). arXiv:1602.09058. Accepted by *Phys. Lett. B*.
- [37] ATLAS Collaboration, “Search for new phenomena in final states with an energetic jet and large missing transverse momentum in pp collisions at $\sqrt{s} = 13$ TeV using the ATLAS detector”, arXiv:1604.07773. Submitted to *Phys. Rev. D*.
- [38] CMS Collaboration, “Search for supersymmetry in the multijet and missing transverse momentum final state in pp collisions at 13 TeV”, (2016). arXiv:1602.06581. Accepted by *Phys. Lett. B*.
- [39] CMS Collaboration, “Search for new physics with the M_{T2} variable in all-jets final states produced in pp collisions at $\sqrt{s} = 13$ TeV”, (2016). arXiv:1603.04053. Submitted to *JHEP*.
- [40] P. J. Fox, R. Harnik, R. Primulando, and C.-T. Yu, “Taking a Razor to Dark Matter Parameter Space at the LHC”, *Phys. Rev. D* **86** (2012) 015010, doi:10.1103/PhysRevD.86.015010, arXiv:1203.1662.
- [41] O. Buchmueller, S. A. Malik, C. McCabe, and B. Penning, “Constraining Dark Matter Interactions with Pseudoscalar and Scalar Mediators Using Collider Searches for Multijets plus Missing Transverse Energy”, *Phys. Rev. Lett.* **115** (2015), no. 18, 181802, doi:10.1103/PhysRevLett.115.181802, arXiv:1505.07826.
- [42] L. Randall and D. Tucker-Smith, “Dijet Searches for Supersymmetry at the Large Hadron Collider”, *Phys. Rev. Lett.* **101** (2008) 221803, doi:10.1103/PhysRevLett.101.221803, arXiv:0806.1049.
- [43] CMS Collaboration, “The CMS experiment at the CERN LHC”, *JINST* **3** (2008) S08004, doi:10.1088/1748-0221/3/08/S08004.
- [44] J. Alwall et al., “The automated computation of tree-level and next-to-leading order differential cross sections, and their matching to parton shower simulations”, *Journal of High Energy Physics* **07** (2014) 079, doi:10.1007/JHEP07(2014)079, arXiv:1405.0301.
- [45] S. Alioli, P. Nason, C. Oleari, and E. Re, “A general framework for implementing NLO calculations in shower Monte Carlo programs: the POWHEG BOX”, *JHEP* **06** (2010) 043, doi:10.1007/JHEP06(2010)043, arXiv:1002.2581.
- [46] E. Re, “Single-top Wt -channel production matched with parton showers using the POWHEG method”, *Eur. Phys. J. C* **71** (2011) 1547, doi:10.1140/epjc/s10052-011-1547-z, arXiv:1009.2450.
- [47] R. Gavin, Y. Li, F. Petriello, and S. Quackenbush, “W Physics at the LHC with FEWZ 2.1”, *Comput. Phys. Commun.* **184** (2013) 208, doi:10.1016/j.cpc.2012.09.005, arXiv:1201.5896.

- [48] R. Gavin, Y. Li, F. Petriello, and S. Quackenbush, “FEWZ 2.0: A code for hadronic Z production at next-to-next-to-leading order”, *Comput. Phys. Commun.* **182** (2011) 2388, doi:10.1016/j.cpc.2011.06.008, arXiv:1011.3540.
- [49] T. Melia, P. Nason, R. Rontsch, and G. Zanderighi, “ W^+W^- , WZ and ZZ production in the POWHEG BOX”, *JHEP* **11** (2011) 078, doi:10.1007/JHEP11(2011)078, arXiv:1107.5051.
- [50] C. M. and A. Mitov, “Top++: A program for the calculation of the top-pair cross-section at hadron colliders”, *Comput. Phys. Commun.* **185** (2014) 2930, doi:10.1016/j.cpc.2014.06.021, arXiv:1112.5675.
- [51] S. Alioli, P. Nason, C. Oleari, and E. Re, “NLO single-top production matched with shower in POWHEG: s- and t-channel contributions”, *JHEP* **09** (2009) 111, doi:10.1088/1126-6708/2009/09/111, arXiv:0907.4076.
- [52] S. Agostinelli et al., “GEANT4 — a simulation toolkit”, *Nucl. Instr. and Meth. A* **506** (2003) 250, doi:10.1016/S0168-9002(03)01368-8.
- [53] T. Sjöstrand et al., “An Introduction to PYTHIA 8.2”, *Comput. Phys. Commun.* **191** (2015) 159, doi:10.1016/j.cpc.2015.01.024, arXiv:1410.3012.
- [54] W. Beenakker, R. Höpker, M. Spira, and P. M. Zerwas, “Squark and gluino production at hadron colliders”, *Nucl. Phys. B* **492** (1997) 51, doi:10.1016/S0550-3213(97)00084-9.
- [55] A. Kulesza and L. Motyka, “Threshold Resummation for Squark-Antisquark and Gluino-Pair Production at the LHC”, *Phys. Rev. Lett.* **102** (2009) 111802, doi:10.1103/PhysRevLett.102.111802.
- [56] A. Kulesza and L. Motyka, “Soft gluon resummation for the production of gluino-gluino and squark-antisquark pairs at the LHC”, *Phys. Rev. D* **80** (2009) 095004, doi:10.1103/PhysRevD.80.095004.
- [57] W. Beenakker et al., “Soft-gluon resummation for squark and gluino hadroproduction”, *JHEP* **09** (2009) 041, doi:10.1088/1126-6708/2009/12/041.
- [58] W. Beenakker et al., “Squark and gluino hadroproduction”, *Int. J. Mod. Phys. A* **26** (2011) 2637, doi:10.1142/S0217751X11053560.
- [59] C. Borschensky et al., “Squark and gluino production cross sections in pp collisions at $\sqrt{s} = 13, 14, 33$ and 100 TeV”, *Eur. Phys. J. C* **74** (2014) 3174, doi:10.1140/epjc/s10052-014-3174-y, arXiv:1407.5066.
- [60] CMS Collaboration, “The fast simulation of the CMS detector at LHC”, *J. Phys. Conf. Ser.* **331** (2011) 032049, doi:10.1088/1742-6596/331/3/032049.
- [61] NNPDF Collaboration, “Parton distributions for the LHC Run II”, *JHEP* **04** (2015) 040, doi:10.1007/JHEP04(2015)040, arXiv:1410.8849.
- [62] CMS Collaboration, “Particle-flow event reconstruction in CMS and performance for jets, taus, and E_T ”, CMS Physics Analysis Summary CMS-PAS-PFT-09-001, 2009.
- [63] CMS Collaboration, “Commissioning of the particle-flow event with the first LHC collisions recorded in the CMS detector”, CMS Physics Analysis Summary CMS-PAS-PFT-10-001, 2010.

- [64] CMS Collaboration, “Performance of photon reconstruction and identification with the CMS detector in proton-proton collisions at $\sqrt{s} = 8$ TeV”, *JINST* **10** (2015) P08010, doi:10.1088/1748-0221/10/08/P08010, arXiv:1502.02702.
- [65] CMS Collaboration, “Performance of electron reconstruction and selection with the CMS detector in proton-proton collisions at $\sqrt{s} = 8$ TeV”, *JINST* **10** (2015) P06005, doi:10.1088/1748-0221/10/06/P06005, arXiv:1502.02701.
- [66] CMS Collaboration, “Performance of CMS muon reconstruction in pp collision events at $\sqrt{s} = 7$ TeV”, *JINST* **7** (2012) P10002, doi:10.1088/1748-0221/7/10/P10002, arXiv:1206.4071.
- [67] M. Cacciari, G. P. Salam, and G. Soyez, “The anti- k_t jet clustering algorithm”, *JHEP* **04** (2008) 063, doi:10.1088/1126-6708/2008/04/063, arXiv:0802.1189.
- [68] M. Cacciari and G. P. Salam, “Pileup subtraction using jet areas”, *Phys. Lett. B* **659** (2008) 119, doi:10.1016/j.physletb.2007.09.077, arXiv:0707.1378.
- [69] CMS Collaboration, “Determination of jet energy calibration and transverse momentum resolution in CMS”, *JINST* **6** (2011) P11002, doi:10.1088/1748-0221/6/11/P11002, arXiv:1107.4277.
- [70] CMS Collaboration, “Identification of b-quark jets with the CMS experiment”, *JINST* **8** (2013) P04013, doi:10.1088/1748-0221/8/04/P04013, arXiv:1211.4462.
- [71] CMS Collaboration, “Performance of b-tagging algorithms in 25 ns data at 13 TeV”, CMS Detector Performance Summary CMS-DP-2015-056, 2015.
- [72] CMS Collaboration, “Identification and filtering of uncharacteristic noise in the CMS hadron calorimeter”, *JINST* **5** (2010) T03014, doi:10.1088/1748-0221/5/03/T03014, arXiv:0911.4881.
- [73] CMS Collaboration, “Electromagnetic calorimeter commissioning and first results with 7 TeV data”, CMS Note CMS-NOTE-2010-012, 2010.
- [74] CMS Collaboration, “Missing transverse energy performance of the CMS detector”, *JINST* **6** (2011) P09001, doi:10.1088/1748-0221/6/09/P09001, arXiv:1106.5048.
- [75] Z. Bern et al., “Driving Missing Data at Next-to-Leading Order”, (2011). arXiv:1106.1423.
- [76] CERN, “PHYSTAT Workshop on Statistical Issues Related to Discovery Claims in Search Experiments and Unfolding”. CERN, Geneva, (2011). doi:10.5170/CERN-2011-006.
- [77] J. Alwall, P. Schuster, and N. Toro, “Simplified Models for a First Characterization of New Physics at the LHC”, *Phys. Rev. D* **79** (2009) 075020, doi:10.1103/PhysRevD.79.075020.
- [78] J. Alwall, M.-P. Le, M. Lisanti, and J. G. Wacker, “Model-independent jets plus missing energy searches”, *Phys. Rev. D* **79** (2009) 015005, doi:10.1103/PhysRevD.79.015005.
- [79] D. Alves et al., “Simplified models for LHC new physics searches”, *J. Phys. G* **39** (2012) 105005, doi:10.1088/0954-3899/39/10/105005.

- 1088 [80] T. Junk, “Confidence level computation for combining searches with small statistics”,
1089 *Nucl. Instr. and Meth. A* **434** (1999) 435, doi:10.1016/S0168-9002(99)00498-2.
- 1090 [81] A. L. Read, “Presentation of search results: the CL_s technique”, *J. Phys. G* **28** (2002) 2693,
1091 doi:10.1088/0954-3899/28/10/313.
- 1092 [82] G. Cowan, K. Cranmer, E. Gross, and O. Vitells, “Asymptotic formulae for
1093 likelihood-based tests of new physics”, *Eur. Phys. J. C* **71** (2011) 1554,
1094 doi:10.1140/epjc/s10052-011-1554-0.
- 1095 [83] S. Chatrchyan et al., “Search for top-squark pair production in the single-lepton final
1096 state in pp collisions at $\sqrt{s} = 8$ TeV”, *Eur. Phys. J. C* **73** (2013) 2677,
1097 doi:10.1140/epjc/s10052-013-2677-2.